Master Thesis

Investigating the Planetary Boundary Layer Height at the CLOUDLAB Field Site

Heather Corden

21-123-617

Oeschger Centre for Climate Change Research

Faculty of Science, University of Bern

Supervisor: PD Dr. Gunter Stober
Atmospheric Dynamics and Meteor Physics
Institute of Applied Physics, University of Bern

Co-Supervisor: Dr. Robert Spirig
Atmospheric Physics
Institute for Atmospheric and Climate Sciences, ETH Zürich

March 2023

Abstract

The planetary boundary layer height (PBLH) is a key parameter for air quality control, visibility forecasting, and for understanding turbulent exchange between the surface and the atmosphere. In the CLOUDLAB project, the PBLH is of interest for ice nucleating particle concentrations during cloud seeding experiments, and for method and instrument performance. The CLOUDLAB field site (Eriswil Rapier-Platz, 47.071°N, 7.874°E) is situated at 920 m above sea level in rolling hills. This study therefore provides a test of PBLH detection methods in terrain which is intermediate between ideal horizontally–homogeneous and truly 'complex' mountainous. A large number of methods have been developed to estimate the PBLH and these methods can be applied to measurements from a range of in situ and remote sensing instruments. In this project, thermodynamic PBLH detection methods (elevated temperature inversion, relative humidity gradient, potential temperature gradient, parcel method, surface-based inversion, surface boundary layer detection by the potential temperature gradient) were implemented on profiles measured by radiosondes, unmanned aerial vehicles, and a microwave radiometer. Using backscatter measurements from a ceilometer, two aerosol-based PBLH detection methods were investigated: the open-source research algorithm 'STRATfinder', and the proprietary PBLH algorithm installed on the ceilometer. Instrument and method comparisons were made on a case study basis and systematically for one year of observations. Method performance under different atmospheric conditions was assessed by splitting the comparisons by the time of day relative to sunrise and by the presence of low-level clouds. The manufacturer algorithm showed better agreement to the STRATfinder mixed layer height than to the STRATfinder PBLH, suggesting that the manufacturer algorithm is more representative of the surface boundary layer height than the residual layer height at night. The agreement between thermodynamic methods applied to the microwave radiometer profiles and STRATfinder was poor. The parcel method showed an underestimation of the boundary layer height compared to STRATfinder. When detected, an elevated temperature inversion was found to be a robust indicator of the boundary layer height that agreed well with STRATfinder. However, the smooth low-resolution profiles of the microwave radiometer often failed to detect an elevated inversion when this was detected by the radiosondes or unmanned aerial vehicles. The profiles from the unmanned aerial vehicles were able to detect the same thermodynamic PBLH signatures as the radiosondes, but only when the flights reached a sufficient altitude. Case study analysis revealed that an ideal diurnal evolution of the boundary layer occurs rarely at the field site and that the presence of low-level clouds leads to large differences between the PBLH detected by thermodynamic and aerosol methods. However, splitting the method comparisons by the time of day or removing time points with low-level clouds did not lead to a large increase in method agreement.

Contents

List of Figures **III**

List of Tables **IV**

Acronyms **V**

1 Introduction **1**
1.1 Motivation and Outline . . . 1
1.2 The Planetary Boundary Layer . . . 2
1.2.1 Diurnal Cycle . . . 2
1.2.2 Boundary Layer Height Definitions . . . 3
1.2.3 Complex Terrain . . . 3
1.2.4 Climatology of the Boundary Layer . . . 4
1.2.5 Comparison with Models . . . 4

2 Methods: Theory and Literature Review **5**
2.1 Backscatter Profile Methods . . . 5
2.1.1 Ceilometer Manufacturer Algorithm . . . 5
2.1.2 STRATfinder Algorithm . . . 5
2.2 Thermodynamic Profile Methods . . . 6
2.2.1 Elevated Temperature Inversion Method . . . 6
2.2.2 Relative Humidity Gradient Method . . . 6
2.2.3 Potential Temperature Gradient Method . . . 6
2.2.4 Parcel Method . . . 7
2.2.5 Richardson Number Method . . . 7
2.2.6 Nocturnal Surface Boundary Layer Detection . . . 7
2.3 Other Methods . . . 8
2.4 Intercomparison of Methods . . . 8

3 Data **10**
3.1 Field Site . . . 10
3.2 Instrumentation . . . 12
3.2.1 Radiosondes . . . 12
3.2.2 Unmanned Aerial Vehicles . . . 13
3.2.3 Microwave Radiometer . . . 14
3.2.4 Automatic Lidar and Ceilometer . . . 14
3.3 Data Availability . . . 15

4 Methods: Implementation **16**
4.1 Backscatter Profile Methods . . . 16
4.1.1 Ceilometer Manufacturer Algorithm . . . 16
4.1.2 STRATfinder Algorithm . . . 16
4.2 Thermodynamic Profile Methods . . . 16
4.2.1 Elevated Temperature Inversion Method . . . 17
4.2.2 Relative Humidity Gradient Method . . . 17
4.2.3 Potential Temperature Gradient Method . . . 17
4.2.4 Parcel Method . . . 17

4.2.5 Richardson Number Method . . . 17
4.2.6 Nocturnal Surface Boundary Layer Detection . . . 20
4.3 Method and Instrument Comparisons . . . 22

5 Results and Discussion **24**
5.1 Case Study Days . . . 24
5.2 Backscatter Profile Methods . . . 25
5.2.1 Manufacturer Algorithm . . . 25
5.2.2 STRATfinder Algorithm . . . 27
5.3 Thermodynamic Methods . . . 31
5.3.1 Instrument Comparison: Radiosondes and Unmanned Aerial Vehicles . . . 31
5.3.2 Instrument Comparison: Radiosondes and Microwave Radiometer . . . 33
5.3.3 Method Comparison to STRATfinder . . . 35

6 Conclusion **40**

Acknowledgements **42**

References **42**

Appendices **45**

A Data **45**
A.1 Unmanned Aerial Vehicle Data . . . 45
A.2 Microwave Radiometer Resolution . . . 46

B Methods **47**
B.1 Hydro-static Pressure Calculation . . . 47
B.2 Relative Humidity Calculation . . . 47
B.3 Richardson Method . . . 48
B.4 Gradient Calculation . . . 49
B.5 STRATfinder Configuration . . . 49
B.6 Statistical Metrics . . . 52

C Results **53**
C.1 Instrument Comparison: Unmanned Aerial Vehicles and Microwave Radiometer . . . 53
C.2 Comparisons Without Low-level Clouds . . . 55

List of Figures

1 Idealised diurnal evolution of the planetary boundary layer 3
2 Location of the CLOUDLAB field site in Canton Bern, Switzerland 10
3 Location and terrain of the CLOUDLAB field site 11
4 Data availability for the project 15
5 Illustration and implementation of the elevated inversion method 18
6 Illustration and implementation of the relative humidity gradient method 18
7 Illustration and implementation of the potential temperature gradient method . . 19
8 Illustration and implementation of the parcel method 19
9 Illustration and implementation of the surface-based inversion method 20
10 Detection of the surface boundary layer top from the potential temperature gradient 21
11 Quality flag distribution for the ceilometer manufacturer algorithm 25
12 Case study days for instrument, method and atmospheric condition comparisons 26
13 Comparison of the planetary boundary layer height estimated by STRATfinder and the ceilometer manufacturer algorithm 29
14 Comparison of the STRATfinder mixed layer height and the ceilometer manufacturer algorithm 30
15 Comparison of planetary boundary layer estimated from radiosonde and unmanned aerial vehicle profiles 32
16 Comparison of surface boundary layer height estimated from radiosonde and unmanned aerial vehicle profiles 32
17 Comparison of the planetary boundary layer height detected from radiosonde and microwave radiometer profiles 34
18 Comparison of the surface boundary layer height detected from radiosonde and microwave radiometer profiles 34
19 Comparison of the STRATfinder planetary boundary layer height and mixed layer height to thermodynamic methods applied to the microwave radiometer 36
20 Comparison of the STRATfinder planetary boundary layer height to the nocturnal surface boundary layer methods applied to microwave radiometer profiles 39
21 Example comparison of unmanned aerial vehicle raw and processed data 45
22 Vertical resolution of the microwave radiometer profiles 46
23 Investigation of smooth gradient methods 50
24 Comparison of planetary boundary layer height estimations detected from microwave radiometer and unmanned aerial vehicle profiles 54
25 Comparison of the surface boundary layer height estimated from unmanned aerial vehicle and microwave radiometer profiles 54
26 Comparison of the planetary boundary layer height estimated by STRATfinder and the ceilometer manufacturer algorithm for times without low clouds 55
27 Comparison of the STRATfinder mixed layer height and the ceilometer manufacturer algorithm planetary boundary layer height for times without low clouds . . 56
28 Comparison of the STRATfinder planetary boundary layer height and mixed layer height to thermodynamic methods applied to the microwave radiometer for times without low clouds 57
29 Comparison of the STRATfinder planetary boundary layer height to the nocturnal surface boundary layer methods applied to microwave radiometer profiles for times without low clouds 58

List of Tables

1 Acronyms used in this thesis V
2 Instruments used in this project 12
3 Thermodynamic methods implemented in this project 21
4 Definitions of the times of day relative to sunrise used for method comparisons . 23
5 Summary of method and instrument comparisons in this project 23
6 Statistical results for STRATfinder planetary boundary layer height and the ceilometer algorithm 28
7 Statistical results for the STRATfinder mixed layer height and the ceilometer manufacturer algorithm planetary boundary layer 28
8 Statistical results for thermodynamic methods implemented on radiosonde and unmanned aerial vehicle profiles 31
9 Statistical results for thermodynamic methods implemented on radiosonde and microwave radiometer profiles 33
10 Statistical results for thermodynamic methods implemented on microwave radiometer profiles and the STRATfinder planetary boundary layer height 37
11 Statistical results for the thermodynamic methods implemented on microwave radiometer profiles and the STRATfinder mixed layer height 38
12 Statistical results for thermodynamic nocturnal surface boundary layer methods applied to microwave radiometer profiles and the STRATfinder mixed layer height 39
13 STRATfinder configuration parameters 51
14 Statistical results for thermodynamic methods implemented on unmanned aerial vehicle and microwave radiometer profiles 53

Acronyms

Atmospheric Structure:	
AGL	Above Ground Level
ASL	Above Sea Level
CBH	Cloud Base Height
CBL	Convective Boundary Layer
EZ	Entrainment Zone
FT	Free Troposphere
MBL	Mountain Boundary Layer
MLH	Mixing Layer Height
PBL	Planetary Boundary Layer
PBLH	Planetary Boundary Layer Height
RL	Residual Layer
SBI	Surface-based Inversion
SBL	Surface Boundary Layer
Times of Day:	
MO	Morning
DT	Daytime
EV	Evening
NT	Nighttime
UTC	Coordinated Universal Time
Measurement Devices:	
ALC	Automatic Lidar and Ceilometer
MWR	Microwave Radiometer
RS	Radiosonde
UAV	Unmanned Aerial Vehicle (Drone)
Physical Variables:	
β	Attenuated Backscatter
RH	Relative Humidity
θ	Potential Temperature
Methods:	
EI	Elevated Inversion
IOP	Intense Observation Period
PM	Parcel Method
RH	Relative Humidity Gradient Method
SBLpT	Surface Boundary Layer Detected by Potential Temperature Gradient
SNR	Signal to Noise Ratio
STRAT	STRATfinder Algorithm
Θ	Potential Temperature Gradient Method
WCT	Wavelet Covariance Transform

Table 1: Acronyms used in this thesis. Note that a distinction is made between the physical variables of potential temperature and relative humidity and the corresponding methods. The definition of the times of day are given in table 4. Instrument-method combinations are referred to in the form instrument/method.

1 Introduction

1.1 Motivation and Outline

The planetary boundary layer (PBL), also referred to as the atmospheric boundary layer, is the bottom-most layer of the atmosphere. It is directly influenced by the Earth's surface and responds to surface forcing within about an hour (Stull, 1988). The flow in the PBL is characterised by turbulence during the day, which means that the PBL is usually well-mixed. This master thesis project investigates the *height* of the planetary boundary layer (PBLH) at the site of the CLOUDLAB field campaign in Eriswil, Canton of Bern, Switzerland.

The PBL is the part of the atmosphere in which humans live. Determining its properties and particularly its height is therefore of great relevance. The PBLH can influence air quality by controlling the volume of air into which pollutants are mixed (Cimini et al., 2020). Knowledge of the PBLH can therefore be used to convert column-mean optical depths measured by satellites into near-surface aerosol concentrations (Emeis et al., 2008). The PBLH has been found to influence noise pollution: low-level temperature inversions can lead to enhanced sound propagation (Emeis et al., 2008). The PBLH can influence local impacts of global climate change as well as the frequency of frost and extreme heat (Zilitinkevich et al., 2012). The influence of PBLH on near-surface visibility means that PBLH measurements are important for airports, insurance companies, and the solar energy sector (Cimini et al., 2020). Measuring the PBLH is especially important for implementing and evaluating PBL processes in weather and climate models (Krishnamurthy et al., 2021), such as the moisture budget for marine PBL clouds (Cadeddu et al., 2023).

The importance of the PBLH motivates the development of methods to estimate the PBLH. Since there is no universal indicator of the PBLH, there is ongoing academic interest in the evaluation and comparison of such methods. The PBLH can be estimated from characteristic properties in vertical profiles of a range of atmospheric variables. These profiles can in turn be measured by a range of instruments, leading to a large number of possible instrument-method combinations (Kotthaus et al., 2023). In light of this, the aims of this project can be summarised as follows:

1. To compare the PBLH estimated by thermodynamic and aerosol methods at the CLOUDLAB field site.

2. To evaluate instrument performance by comparing PBLH estimations using the same method applied to measurements from different instruments.

3. To investigate the atmospheric conditions which lead to differences in the PBLH estimated by different instruments and methods.

To address these three aspects, thermodynamic PBLH detection methods were implemented on measurements from radiosondes (RS), unmanned aerial vehicles (UAVs) and a microwave radiometer (MWR). Aerosol-based PBLH detection methods were implemented on measurements from an automatic lidar and ceilometer (ALC). Specifically, the open-source research algorithm for PBLH tracking, 'STRATfinder', and the proprietary PBLH algorithm installed on the ALC. Instrument and method comparisons were made first on a case study basis and then systematically for one year of observations. Differences in method performance and agreement due to atmospheric conditions were assessed using the case studies and statistical comparisons split by the time of day and the presence of low-level clouds.

Within the CLOUDLAB project, the PBLH is of interest for cloud seeding experiments (see section 3.1): knowledge of the PBLH could help quantify the background level of ice nucleating particles due to mixing from the ground. However, the main interest of this project for the wider CLOUDLAB project is the evaluation of instrument performance under different atmospheric conditions. A large number of existing studies investigate the PBLH using in situ and remote sensing instruments (see for example the review by Kotthaus et al., 2023). This project applies and evaluates methods introduced in previous studies, with a number of novel aspects:

1. The measurement of the PBLH using profiles from UAVs.
2. The hilly topography surrounding the field site, which is intermediate between the flat terrain and highly complex mountainous terrain investigated in previous studies
3. A dataset with RS and UAV profiles principally taken in winter, nocturnal, cloudy conditions when the boundary layer is expected to be harder to detect.

The remainder of this section describes the PBL structure and characteristics related to this study. Section 2 outlines the theory of the PBLH detection methods used in this study, including a review of previous studies using these methods. Section 3 describes the CLOUDLAB field campaign, instruments and data availability. Section 4 details the technical implementation of the methods. The results are presented and discussed in section 5, firstly for case study days (section 5.1) and secondly for systematic instrument and method comparisons.

1.2 The Planetary Boundary Layer

1.2.1 Diurnal Cycle

Under 'ideal' conditions of a warm, cloud-free day, the PBL over flat terrain follows a typical diurnal evolution (figure 1). In the morning, solar heating of the ground leads to upward turbulent heat fluxes and the growth of the convective boundary layer (CBL). The CBL typically reaches its maximum height in the early afternoon (Kotthaus et al., 2023). The CBL is topped by an entrainment zone (EZ), in which turbulent intensity decays with height and tracers are exchanged with the overlying free troposphere (FT) (Seibert et al., 2000). After sunset, radiative cooling of the surface leads to the formation of a stable surface boundary layer (SBL). The SBL is often but not always characterised by a surface-based temperature inversion (SBI), in which the temperature increases upwards away from the now colder surface. The CBL from the previous day becomes decoupled from the surface and is referred to as the residual layer (RL) (Stull, 1988). The RL retains the elevated aerosol concentration from the CBL but typically has a more neutral stratification (Collaud Coen et al., 2014).

The presence of clouds, complex terrain or synoptic-scale forcing can lead to the deviation of the diurnal cycle from this ideal evolution. For example, persistent cold ground temperatures in winter or polar environments can lead to an SBI which persists throughout day and night (Kotthaus et al., 2023; Zilitinkevich et al., 2012). With extensive cloud cover, reduced heat fluxes result in the CBL exhibiting slower growth and a lower maximum height. The CBL development in this case is not driven by solar heating, but by forced mechanical turbulence or radiative cooling at the cloud top (Collaud Coen et al., 2014; Heutte, 2021).

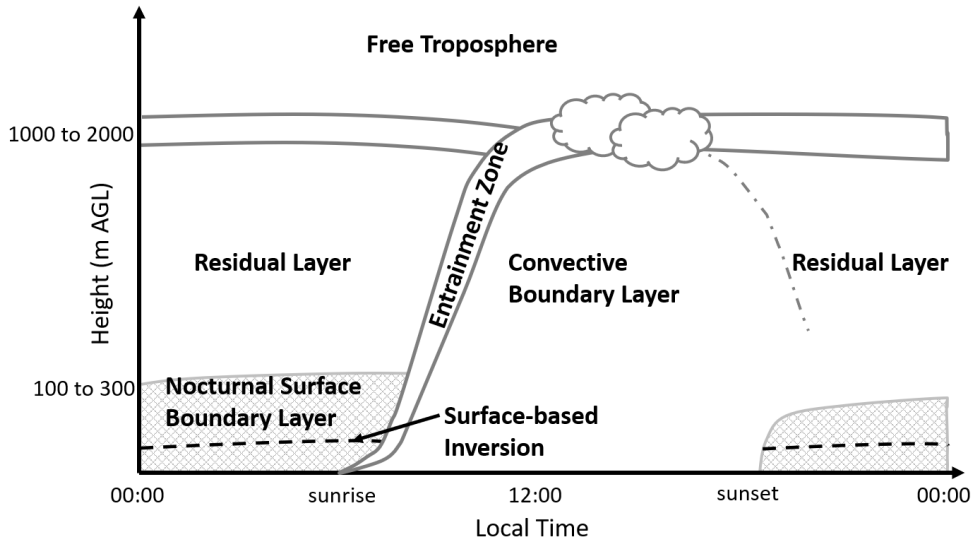

Figure 1: Idealised diurnal evolution of the PBL under cloud-free conditions. Adapted after Collaud Coen et al. (2014) and Bugnard (2023).

1.2.2 Boundary Layer Height Definitions

The first issue when comparing measurements of the PBLH is a definition of the height to be measured. The European Cooperation in Science and Technology (COST) action 710 (harmonisation of the pre-processing of meteorological data for atmospheric dispersion models) defines the *daytime* PBLH as 'the height of the layer adjacent to the ground over which pollutants or any constituents emitted within this layer or entrained into it become vertically dispersed by convection or mechanical turbulence within a time scale of about an hour' (Collaud Coen et al., 2014; Finardi et al., 1998). This corresponds to the mixed layer height (MLH) used by Dang et al. (2019) and Seibert et al. (2000). The latter study emphasises that the MLH corresponds to the *top* of the EZ, though this ambiguity of the finite transition zone between the PBL and the FT is not addressed in many studies. In the ideal nocturnal PBL, pollutants emitted during the night will largely be contained within the SBL (Seibert et al., 2000). In accordance with this and with the STRATfinder algorithm (section 2.1.2), in this project the MLH is assumed to be comparable to the CBL top during the day and the SBL top at night. Hence during the day, the MLH and PBLH should refer to the same height. At night, the MLH refers to the SBL top, whereas the PBLH refers to the RL top. The consistency of different PBLH methods with the above definition is discussed in section 2.2.6.

1.2.3 Complex Terrain

PBL studies have historically concentrated on developing scaling laws for PBL properties for horizontally-homogeneous terrain, such as extensive farmland (Stull, 1988). Complex terrain refers to ground surfaces with irregularities which affect the overlying PBL and can include forests and cities, but typically refers to mountainous areas. There are generally fewer studies investigating the PBLH over complex terrain (Kotthaus et al., 2023). Boundary layer structure in complex terrain may not follow the idealised structure described above. Mountains and valleys can lead to distinct PBL characteristics such as slope winds (Ketterer et al., 2014), cross-valley

vortices (Babić et al., 2021) and long-lasting inversions (Lehner and Rotach, 2018). Where surface in-homogeneity leads to horizontal temperature gradients, 'low level jets' can be common (Cuxart, 2011). To account for the complexity of the PBL structure in mountainous environments, Lehner and Rotach (2018) suggest a specific definition of the mountain boundary layer (MBL), which emphasises the role of the MBL in the exchange of mass, energy and momentum between the mountainous terrain and the FT. Although there have been some campaigns focused on the MBL (such as the MAP project - Rotach and Zardi, 2007), these tend to study valleys and ridges on a larger scale than the rolling hills at Eriswil. A key aim of this project is to investigate the evolution of the PBL and the performance of PBLH algorithms for the 'intermediate' terrain at Eriswil.

1.2.4 Climatology of the Boundary Layer

A number of studies use the comparison of PBLH detection methods as a precursor for the compilation of a PBLH climatology. Seidel et al. (2010) used seven methods applied to RS profiles to compile a 10-year global PBLH climatology. They found that the typical PBLH is between 200 and 2000 m. However, seasonal variations differed between stations and methods, with the seasonal variation often of the same magnitude ($\sim \pm 400$ m) as the uncertainty associated with the choice of method. Seidel et al. (2012) focused on continental Europe and the US using a single method (bulk Richardson number method, see section 2.2.5 and appendix B.3) They found that the PBLH seasonal pattern differed depending on the time of day: daytime PBLH was larger in the summer than the winter, but nighttime PBLH showed the opposite pattern. Collaud Coen et al. (2014) investigated the PBLH for Payerne and Schaffhausen on the Swiss plateau, using RS as well as remote sensing methods. In agreement with Seidel et al. (2012), the CBL height was maximum in summer and minimum in winter. Collaud Coen et al. (2014) also noted that the PBLH appears to follow the annual solar radiation cycle more closely than the mean temperature cycle, with extreme CBL heights occurring at the solstices. Using a range of remote sensing instruments at Payerne, Heutte (2021) showed that the seasonality of the daytime PBLH was less pronounced for cloudy days than clear days. Since only a single year of data was available at the CLOUDLAB field site (section 3.3), a climatology of the PBLH could not be compiled. Instead, the focus here is the comparison of different PBLH detection methods.

1.2.5 Comparison with Models

Few studies compare the observed PBLH with theoretical models. Zilitinkevich et al. (2012) formulate a range of analytical models for the PBLH under ideal convective, stable and neutral conditions, but do not verify these against observations. The SBL can be parameterised using diagnostic or relaxation relations, whereas the CBL requires a prognostic equation to capture the morning growth (Stull, 1988). Seibert et al. (2000) emphasise that numerical constants within such parameterisations are often highly site-specific. Seidel et al. (2012) found that reanalysis data (ERA-interim) and numerical climate models (GFDL AM3 and NCAR CAM5) tend to overestimate PBLH, due to difficulty in simulating stable conditions. Collaud Coen et al. (2014) demonstrated that the COSMO-2 model also overestimates the PBLH, with a bias that is only partially explained by the model PBLH methodology. However, in the complex terrain of the Alps, Ketterer et al. (2014) found that COSMO-2 underestimated the PBLH when compared to measurements from an ALC.

2 Methods: Theory and Literature Review

2.1 Backscatter Profile Methods

The profile of attenuated backscatter β provided by an ALC (see section 3.2.4) can be used to find the PBLH, since β is representative of the aerosol concentration. Under the assumption that the main source of aerosols is the ground and that convection lifts and mixes them homogeneously within the PBL, we expect higher, altitude-independent values of β within the PBL and lower values in the FT above (Foken, 2022). However, a large number of methods exist to detect this change. Two comprehensive reviews are given by Dang et al. (2019) and Kotthaus et al. (2023). Recent algorithms such as STRATfinder have moved away from detecting the PBLH from backscatter profiles at single time points and towards using a combination of methods and temporal layer tracking (Kotthaus et al., 2020). Since aerosol concentrations are a result of *previous* mixing processes, their vertical distribution may not be representative of the current state of the PBL (Kotthaus and Grimmond, 2018). At night, this can result in the detection of the top of the RL rather than the SBL (Kotthaus and Grimmond, 2018). In addition, energetic overshooting plumes in the CBL can transport aerosols above the EZ, leading to an overestimation of the PBLH compared to thermodynamic methods (Seibert et al., 2000). Cloud boundaries within the PBL can be falsely identified as the PBLH by aerosol methods, as both are regions of strong backscatter changes.

2.1.1 Ceilometer Manufacturer Algorithm

The proprietary algorithm of the ALC is based on the wavelet covariance transform (WCT) method (Lufft, 2016). However, the details of the exact algorithm used are not known. In the WCT method, the PBLH is calculated from the covariance transform between β and a wavelet profile. The wavelet is chosen to match the expected β signal from a region of strong aerosol concentration change (Dang et al., 2019; Morille et al., 2007). Rieutord et al. (2021) found that a WCT-based manufacture algorithm (for a different lidar system) performed well without prior tuning. The WCT method may fail at detecting the spring and summer daytime PBLH, due to the high variability of the aerosol signal in the region of the CBL top. The method can also be sensitive to the scale of the wavelet used (Emeis et al., 2008). Despite a lack of transparency about such parameters, the manufacturer algorithm returns a PBLH automatically with the ALC data and has the potential to be a convenient operational PBLH detection method. It was therefore evaluated against the STRATfinder algorithm in this project.

2.1.2 STRATfinder Algorithm

STRATfinder is an open-source PBLH algorithm which combines elements from the previous algorithms STRAT-2D/STRAT+ and pathfinderTURB (Kotthaus et al., 2020). Layer boundaries in the β profile are traced over time using a 'pathfinder' approach, whereby the optimal path in a field of weights is found by minimising a cost function (Dijkstra's algorithm). The weights are calculated based on two methods which have themselves been used for PBLH detection (Dang et al., 2019; Foken, 2022). Firstly, the vertical gradient of β is considered, with a large magnitude negative vertical gradient corresponding to a low weight. A second layer of weights is calculated from the temporal variance of β, with a high variance corresponding to a low weight. A high variance is expected at the EZ, due to the combination of updrafts of high aerosol concentration PBL air and downdrafts of low aerosol concentration air from the FT (Dang et al., 2019; Emeis et al., 2008). The layer heights are tracked using a decision tree based on the ideal daily evolution

(section 1) and user-defined search regions (appendix B.5). Importantly, STRATfinder returns both a PBLH (referred to as STRAT/PBLH) and an MLH (STRAT/MLH)(see section 1.2.1). The PBLH detection relies on the weights from the vertical gradient, whereas the MLH detection uses the gradient weights before the morning growth stage and the variance weights between the morning growth onset and midnight.

STRATfinder is evaluated against thermodynamic PBLH estimations derived from the 'Aircraft Meteorological Data Relay' by Kotthaus et al. (2020). The MLH from STRATfinder was found to be smaller than that calculated from the parcel method (PM, see section 2.2.4) during the morning growth phase. The PBLH from STRATfinder and the PM converged to similar peaks in the afternoon, with the two methods agreeing within 300 m around 80% of the time.

2.2 Thermodynamic Profile Methods

'Thermodynamic' methods refer to methods applied to profiles of temperature, humidity and pressure measured by RS, UAVs or the MWR. The implementation of these methods in my project is described in section 4. Apart from the parcel method (PM), method acronyms refer to the specific implementation in my study (table 3) so are not used in this section.

2.2.1 Elevated Temperature Inversion Method

Although methods using the potential temperature θ are more common than those using the temperature T, the latter has the advantage that no pressure measurements are required . If the PBL is topped by an elevated temperature inversion , the base of this inversion forms a cap on mixing and can be considered as the PBLH. However, not all soundings feature such an inversion (Seidel et al., 2010). At night, an elevated inversion is likely to be associated with the top of the RL rather than the SBL (Kotthaus and Grimmond, 2018). A second near-surface inversion (SBI) may also be present and is discussed in section 2.2.6.

2.2.2 Relative Humidity Gradient Method

Assuming that the PBL is well-mixed, the relative humidity RH in the PBL is expected to be more spatially uniform and higher than that in the FT. The minimum in the vertical gradient of RH can be therefore be associated with the CBL top in the day and the RL at night (Collaud Coen et al., 2014; Li et al., 2021). RH methods are used less frequently than methods for other thermodynamic variables. A possible reason for this is the uncertainty associated with humidity measurements, both for the capacitive sensors in RS and humidity retrievals from MWRs. In addition, methods using RH are liable to false attribution of cloud tops as the PBLH, since these are regions of sharp RH decreases (Seidel et al., 2010; Wang and Wang, 2014).

2.2.3 Potential Temperature Gradient Method

The potential temperature θ is the temperature an air parcel would have if brought adiabatically to a reference pressure p_0. It is calculated from the temperature T and pressure p according to

$$\theta = T \left(\frac{p_0}{p} \right)^{\frac{R_d}{c_p}}, \tag{1}$$

where R_d is the gas constant for dry air and c_p is the specific heat capacity of dry air at constant pressure (Stull, 1988). The vertical potential temperature gradient $\frac{d\theta}{dz}$ indicates the stability of

the atmosphere to vertical motion: increasing θ with height implies that air parcels displaced upwards will be cooler and denser than surrounding parcels and will sink back towards their original position, resulting in a stable atmosphere, whereas decreasing θ with height implies instability to vertical motion. The FT is typically more stably stratified than either the CBL or the RL. The PBLH can therefore be detected from an increase in $\frac{d\theta}{dz}$, either using an absolute threshold (Li et al., 2021) or by detecting a maximum peak in $\frac{d\theta}{dz}$ (Martucci et al., 2007). Seidel et al. (2010) found that this method gave a systematically higher PBLH than temperature inversions or the PM applied to RS data.

2.2.4 Parcel Method

The two most common thermodynamic methods to determine the daytime PBLH are the PM and Richardson number method (Kotthaus et al., 2023). The PM defines the PBLH as the height to which an air parcel can rise adiabatically from the surface (Li et al., 2021; Seibert et al., 2000). This corresponds to the height at which the measured temperature profile crosses the dry adiabat. Equivalently, the height where θ is equal to the surface potential temperature θ_0. Some authors use an 'advanced parcel method', whereby a small excess is added to the θ_0, proportional to the measured heat flux. However, Seibert et al. (2000) concluded that this excess would be outweighed by stochastic fluctuations in θ_0. The PM is only suitable for unstable conditions in which θ initially decreases with height.

2.2.5 Richardson Number Method

The Richardson method is commonly used operationally and within numerical weather models (Collaud Coen et al., 2014). Since no results from the Richardson method were analysed in my project (see section 4.2.5), the method is described and reviewed in appendix B.3.

Both the PM and Richardson number method rely on accurate surface temperature measurements. Collaud Coen et al. (2014) found that varying the surface temperature by ± 0.5°C led to variations in the maximum afternoon PBLH measured by both methods of ± 50 to 150 m. Both methods can also be performed using the virtual potential temperature θ_v, which accounts for moist air (Heutte, 2021; Seibert et al., 2000; Seidel et al., 2012; Stull, 1988). Since moisture decreases the density of the air and allows it to convectively rise to higher altitudes, this results in a higher PBLH (by around 3 to 8% as estimated by Collaud Coen et al., 2014). The use of θ_v was not considered in this study, due to a desire to separate PBLH metrics depending on temperature and humidity.

2.2.6 Nocturnal Surface Boundary Layer Detection

The presence of both the SBL and RL (section 1.2.1) leads to ambiguity in the definition and detection of a nocturnal PBLH. If the CBL on the preceding day is sufficiently strong, the change in RH and θ at the RL top is expected to be stronger than that at the SBL top, so the RH and θ gradient methods are expected to detect the RL top rather than the SBL top. An elevated temperature inversion, if present, would also signal the top of the RL. The PM will not be successful at night, due to the stability of the SBL.

The transition between the SBL and RL is typically less distinct than the RL top, but can be estimated from profiles of temperature or θ. If an SBI is identified in the temperature profiles, its top can be used to define the SBL height (Seidel et al., 2010). Since the top of an SBI typically

occurs within 700 m of the ground, accurate SBI detection relies on high resolution data at low heights (Seidel et al., 2010). Bianco et al. (2017) found that profiles from MWR often lack the resolution required to identify an SBI.

At the transition from a stable SBL to a more neutral RL, the decrease in $\frac{d\theta}{dz}$ can be used to measure the height of the SBL. A strict condition of a vanishing $\frac{d\theta}{dz}$ can be used (Collaud Coen et al., 2014), or the detection of local minimum peaks which exceed a threshold value (0.0003 $°Cm^{-1}$ in Li et al. (2021), 0.05 $°Cm^{-1}$ in Heutte, 2021) If vanishing $\frac{d\theta}{dz}$ is required, the detected SBL height will by definition be greater than the SBI height, since the θ gradient will always be positive at the SBI (Collaud Coen et al., 2014).

2.3 Other Methods

The above selection of methods is not exhaustive and concentrates on the instruments available at the field site. Other instruments for which PBLH detection method have been developed include SODAR, Doppler wind radar, dual wavelength lidars and flux measurements (Emeis et al., 2008; Kotthaus et al., 2023; Turner and Lohnert, 2021). A recent technique which can be applied to different continuous measurement devices is edge detection. This uses image processing techniques to identify the abrupt change in atmospheric properties between the PBL and FT (Dang et al., 2019; Pan et al., 2021).

Machine learning is increasingly being used to estimate the PBLH by combining different observations (Kotthaus et al., 2023). For example, detection of the PBLH can be implemented as a random forest regression model linking lidar backscatter features to the PBL top (Krishnamurthy et al., 2021), or as a classification problem of points inside and outside the PBL (Rieutord et al., 2021). However, due to the lack of a universal standard for the PBLH, the results of these efforts are strongly dependent on the PBLH used to train the algorithm (Krishnamurthy et al., 2021). Machine learning methods are outside the scope of this project.

2.4 Intercomparison of Methods

A comparison of PBLH detection methods is fundamentally challenging for a number of reasons. Firstly, the PBL is a dynamic layer whose height changes in time and space. The transition to the FT does not occur at one height, but over a finite transition region. Furthermore, there is no universal standard for measuring the PBLH. Whilst RS are often used as the de facto standard, the many thermodynamic methods to extract the PBLH from RS profiles do not always give consistent heights (Li et al., 2021). Different methods assess different properties of the PBL. Thermodynamic methods assess the *current* stability of the PBLH, which affects current mixing processes. Heights derived from aerosol or *RH* profiles asses the current mixed state of the PBL, which arises as a result of *previous* mixing processes. Aerosol concentrations are influenced by horizontal advection in addition to the stability of the local PBL (Seibert et al., 2000). Furthermore, local atmospheric conditions can result in site-specific biases between instruments and methods (Cadeddu et al., 2023; Martucci et al., 2007). This reduces the feasibility of 'universal' PBLH algorithms. An additional difficulty arises in the desire to separate differences arising from the instrument used to acquire a profile and the method applied to that profile. Uncertainties in layer detection are closely linked to uncertainties in the atmospheric profiles, including near-surface measurements and vertical resolution (Kotthaus et al., 2023).

Nevertheless, many studies have made careful comparisons of different instrument-method combinations (Aryee et al., 2020; Collaud Coen et al., 2014; Li et al., 2021; Wang and Wang, 2014). Methods can be compared pairwise for all possible combinations, or by assigning one method to be a 'standard' against which all other methods are compared (Seibert et al., 2000). Aryee et al. (2020) used a standard determined by consistency between methods: the PBLH was defined as the lowest height where three of four variables simultaneously met the criteria for the PBLH. Different studies use different methods for comparison: linear regression, histograms of absolute differences, box plots, correlation coefficients, root mean square error, mean absolute error and statistical tests to identify the significance of differences (Aryee et al., 2020; Collaud Coen et al., 2014; Li et al., 2021; Seibert et al., 2000; Seidel et al., 2010). Some studies also attempt to find the uncertainty associated with different methods, such as assessing the width of detected peaks in a profile (Collaud Coen et al., 2014; Heutte, 2021; Seidel et al., 2010).

Amongst the thermodynamic methods, extreme gradient indicators have been found to agree better than methods identifying elevated temperature inversions or using the PM (Aryee et al., 2020; Li et al., 2021; Seidel et al., 2010). The PM and Richardson number method show high agreement (Seibert et al., 2000), as expected from the similarity of the methods (see appendix B.3). RH and θ gradient methods have been found to give higher PBLH estimates (Seidel et al., 2010), whereas the PM generally gives lower heights (Li et al., 2021; Seidel et al., 2010). However, Collaud Coen et al. (2014) concluded that the PM applied to MWR data was the most 'robust' method for operational PBL detection, due to good performance under a range of meteorological conditions and the ability to track the diurnal cycle.

The comparison between methods can be subdivided to assess the performance at different times of day (Bianco et al., 2017; Collaud Coen et al., 2014), in different seasons (Seidel et al., 2012) or for different near-surface stabilities (Li et al., 2021; Martucci et al., 2007; Seibert et al., 2000). Methods generally show greater agreement under daytime convective conditions than under stable or nocturnal conditions (Kotthaus et al., 2023; Li et al., 2021). Performance variation under different stabilities (and hence at different times of day) has led to some authors recommending operational regimes in which different methods are used at certain times of day (Li et al., 2021). For RS profiles, Li et al. (2021) recommend the θ and Richardson number methods for the CBL and the θ gradient and RH gradient methods for the SBL. Seibert et al. (2000) recommend the PM for the CBL and the Richardson number method for the SBL. The variation of these recommendations illustrates once more the issue of finding a common PBLH under all meteorological conditions.

Cloudy and rainy conditions pose additional challenges for PBLH detection and lead to decreased method agreement (Collaud Coen et al., 2014). Firstly, the diurnal evolution of the PBL is less pronounced (section 1.2.1). Secondly, clouds and rain affect the measurement of atmospheric properties by different instruments. For an MWR, scattering of thermal radiation off cloud and rain droplets leads to increased uncertainty in temperature and humidity profiles, and the PBLH measurements derived from them (Bianco et al., 2017; Dang et al., 2019). For aerosol and RH methods, cloud boundaries within the PBL can be falsely identified as the PBLH. Low clouds can also cause an ambiguity in the PBLH definition: if the low cloud has been advected from another location, the lowest layer of the atmosphere can no longer be described as being directly influenced by the ground surface. Wang and Wang (2014) make a distinction between clouds containing stable layers, which suppress pollutant dispersal so should define the PBLH, and clouds without stable layers, for which other thermodynamic PBLH indicators should be used.

3 Data

3.1 Field Site

CLOUDLAB is a project of the Institute for Atmospheric and Climate Sciences at ETH Zürich, which investigates cloud processes and precipitation formation using laboratory experiments, field observations and numerical modelling (`https://cloudlab.ethz.ch/`). The field site is located at Eriswil Rapier-Platz (47.071°N, 7.874°E, 920 m ASL, figure 2) where wintertime stratus clouds serve as a natural laboratory for seeding experiments. The main field site sits on an exposed hill in grazed farmland (figure 3). An ALC, MWR and automatic surface weather station have been operating continuously at the site since January 2022 (table 2 and section 3.3).

During the winter (December to February), cloud seeding experiments are performed in 'intense observation periods' (IOPs), which typically last for one night. The required conditions for an IOP are sufficiently cold temperatures (the −5°C level should lie below 1.5 km AGL), consistent winds (typically northeasterly 'Bise') and the presence of clouds. It is expected that this will occur around 30 times in each winter campaign. During an IOP, RS, UAVs and a tethered balloon provide additional measurements. The data from the tethered balloon were not used in this project. Additional remote sensing instruments including a wind profiler and Doppler lidar were only installed for the 2022-23 field season, and were therefore not considered in this project.

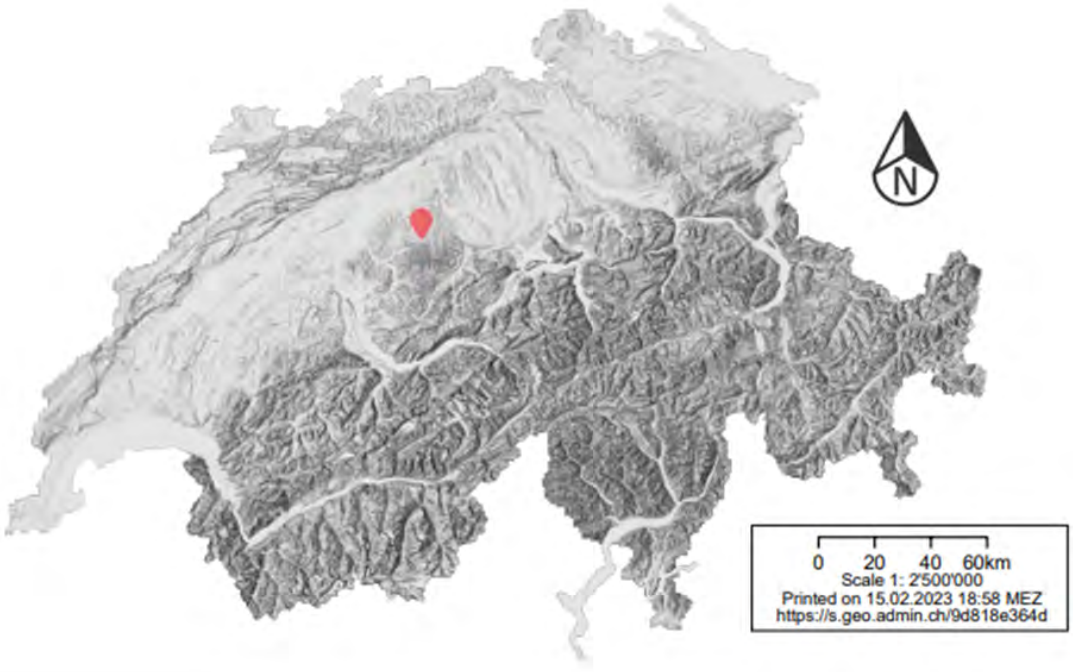

Figure 2: The location of the CLOUDLAB field site (red marker, 47.071°N, 7.874°E) in Canton Bern, Switzerland. Map data from https://map.geo.admin.ch/ (accessed 15/2/2023).

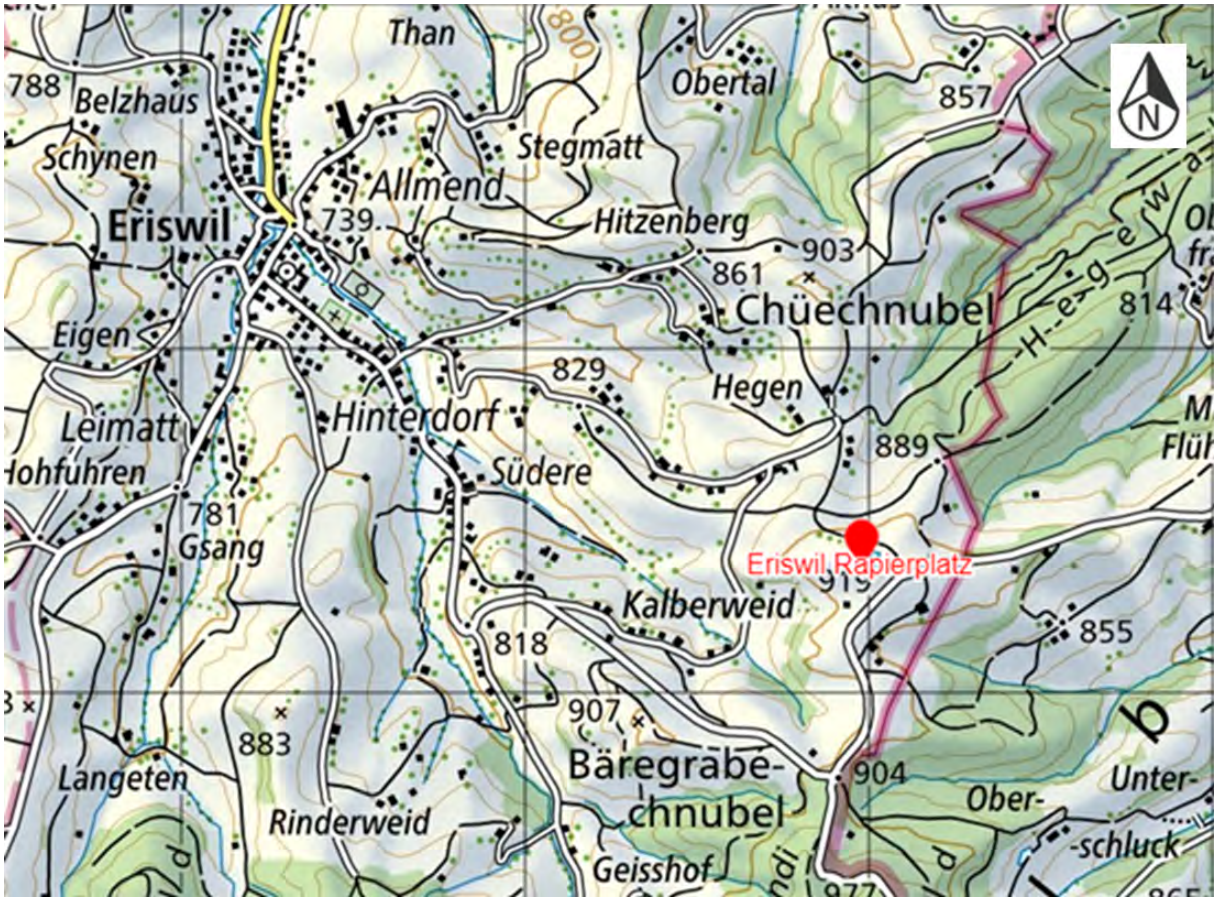

(a)

(b)

(c)

Figure 3: Location and terrain of the CLOUDLAB field site. (a) The field site (Eriswil Rapier-Platz, red marker) in relation to the village Eriswil. The grid distance is 1 km and isohypses are spaced at 20 m. Map data from https://map.geo.admin.ch/ (accessed 15/2/2023). (b) Aerial photograph of the field site, orientated with north at the top of the photo. (c) Instrument arrangement at the field site, looking north. From left to right: tethered balloon preparing for launch, winch used to bring the balloon back to the ground, trailer with the MWR on the roof, ALC, cloud radar, data processing trailer, wind profiler, container with remote sensing instruments from the Leibniz Institute for Tropospheric Research (not used in this project).

3.2 Instrumentation

Instrument	**Model, Manufacturer**	**Variables**	**Vertical Resolution**	**Data Availability**
Radiosonde (RS)	Sparv S1H3, Windsond	Temperature T Relative Humidity RH Pressure P Wind Direction ϕ Wind Speed $\lvert\vec{V}\rvert$	$\sim$ 20 m	*typically two launches per IOP*
Unmanned Aerial Vehicle (UAV, Drone)	MM-670, Meteomatics	Temperature T Relative Humidity RH Pressure P Wind Direction ϕ Wind Speed $\lvert\vec{V}\rvert$	*varies by climb-speed* Resampled to 5 m	*typically two launches per IOP*
Automatic Surface Weather Station	WXT536, Vaisala	Temperature T Relative Humidity RH Pressure P Wind Direction ϕ Wind Speed $\lvert\vec{V}\rvert$ Rain Flag	-	*continuous* (every 1 s)
Automatic Lidar and Ceilometer (ALC)	CHM15K, Lufft	Attenuated Backscatter β	15 m	*continuous* (every 15 s)
Microwave Radiometer (MWR)	HATPRO G5, Radiometer Physics GmbH	Temperature T Relative Humidity RH Absolute Humidity ρ_v	*varies with height*: See figure 22	*continuous* (every 1 minute for 10 minutes on, 10 minutes off)

Table 2: Instruments used in this project. The automatic surface weather station is attached to the MWR. The rain flag indicates whether it is raining or not.

3.2.1 Radiosondes

The PBLH has historically been measured with thermodynamic profiles from RS. In situ measurements are made by a sensor lifted by a helium balloon. RS profiles have a high vertical resolution and offer simultaneous measurements of multiple atmospheric variables (table 2). The global network of stations which regularly launch RS and the long time series of such measurements make RS suitable for PBLH climatology studies (Dang et al., 2019; Kotthaus et al., 2023; Seidel et al., 2012). PBLH measurements from RS profiles are often chosen as standards, against which alternative instruments and methods are compared (Collaud Coen et al., 2014; Kotthaus et al., 2023; Morille et al., 2007). In addition, they are increasingly used as training data for machine learning PBLH algorithms (Li et al., 2021; Rieutord et al., 2021). However,

the fact that typically only two RS are launched per day means that they cannot be used to track the diurnal cycle of the PBLH. Furthermore, sensor lag may lead to smoothing of profiles (Seibert et al., 2000) and horizontal movement of the balloon during ascent can result in measurements which are not representative of the column above the launch site (Kotthaus et al., 2023).

At the field site, RS are only launched during an IOP, to investigate the wind conditions required for cloud seeding. RS profiles meeting the following conditions were maintained for the analysis:

1. Data from the temperature, pressure and humidity sensors must be available for the duration of the flight (this particularly excluded flights with faulty pressure sensors)
2. The maximum height reached must be greater than or equal to 2000 m ASL
3. The first height at which data is available must be below 1200 m ASL

These conditions are stricter than those used for the UAV profiles (section 3.2.2). The motivation for this was to generate as 'clean' a RS dataset as possible, against which the PBLH estimations from the UAVs and MWR could be compared. A higher maximum height threshold was also considered. However, for the four short profiles with a maximum height greater than 2000 m but lower than 3000 m, the PBLH detected by other RS launched within 3 hours were smaller than the maximum height reached by the short profiles. The short profiles were therefore assumed to reach a sufficient height to detect the PBLH and were not rejected.

3.2.2 Unmanned Aerial Vehicles

The use of UAVs for atmospheric profiling is relatively novel (Kotthaus et al., 2023). The UAVs use similar sensors to RS and produce profiles with a high vertical resolution. In the future, the ability to launch UAVs automatically may lead to increased data availability compared to RS for operational PBL monitoring.

Two different UAVs are used at the field site, but these are not distinguished in this project. As with the RS, UAVs are only launched during an IOP. To exclude horizontal cloud seeding flights and short profiles, only UAV flights meeting the following requirements were included in the analysis:

1. The latitude and longitude must not change by more than 0.0001 deg during the flight
2. The maximum height reached must be greater than or equal to 1250 m ASL

A lower maximum height threshold was used compared to the RS ascents, in order to maintain a greater number of ascents. The issue of the flight maximum altitude being smaller than the PBLH is discussed further in section 4.3. The UAVs return both raw sensor data at a frequency of 20 Hz as well as data processed by a proprietary algorithm. After initial investigations, I decided to use the raw data in this project for increased transparency in the processing steps taken (appendix A.1). The raw data was aggregated by taking the median measurement in each 5 m interval. In addition, only measurements from the ascent were used.

3.2.3 Microwave Radiometer

An MWR is a passive remote sensing instrument which measures thermal emission from the atmosphere (Foken, 2022). The measured spectral radiance is converted to a vertical profile of brightness temperature. Height information is obtained using weighting functions applied to multiple frequency channels: at different frequencies (specifically, at different distances from the oxygen absorption complex), the atmosphere is more transparent, so some channels receive information from further afield (Radiometer Physics GmbH, 2014). Alternatively, the height can be determined by scanning the atmosphere at different angles (Radiometer Physics GmbH, 2014). The brightness temperature is converted to atmospheric variables using calibrated algorithms. Recent algorithms use neural networks based on either long term records of RS or reanalysis data. For temperature measurements, MWR profiles have been found to agree with RS profiles to within 0.5 to 2.0 °C root mean square error (Kotthaus et al., 2023). The key advantage of an MWR compared to RS and UAVs is the continuous operation, allowing the diurnal cycle of the PBLH to be tracked. However, the vertical resolution decreases with height and the retrievals are less accurate in rain due to scattered radiation (Bianco et al., 2017; Collaud Coen et al., 2014; Dang et al., 2019). For PBLH estimations, Heutte (2021) found that the MWR at Payerne underestimated the PBLH detected by the PM compared to other remote sensing instruments and attributed this to device overheating.

The MWR at the field site is a HATPRO G5 from Radiometer Physics GmbH. The MWR alternates between a 'zenith' scan, in which height information is obtained from frequency information alone, and an elevation scanning mode. The two scans are combined to form profiles with increased vertical resolution close to the surface (figure 22). The retrieval of atmospheric variables is via a neural network, in which a cost function is minimised using a Davidon–Fletcher–Powell algorithm (Radiometer Physics GmbH, 2014). Reanalysis data (ERA 5) provides the reference data for the neural network. However, the grid size of 30 km means the reanalysis is unlikely to be fully representative of the conditions at Eriswil, in particular relating to the hilly terrain. Humidity profiles only operate in the zenith mode. Since the microwave signal received is proportional to the absolute humidity, the absolute humidity retrievals are considered to be more 'natural' than RH retrievals (Radiometer Physics GmbH, 2008). In this project, RH was therefore calculated from the absolute humidity and the temperature (appendix B.2).

3.2.4 Automatic Lidar and Ceilometer

ALCs were initially developed to detect cloud base heights but are increasingly being used for PBLH studies (Kotthaus and Grimmond, 2018). A near-infrared laser is fired upwards and the resulting backscatter is imaged using an aligned telescope. The pulse travel time and attenuated backscatter β provide information on the vertical distribution of aerosols and cloud droplets (Foken, 2022). ALCs can be preferable to alternative lidar systems due to their lower cost and compact design (Kotthaus and Grimmond, 2018). This has led to them being widely adopted in operational networks, such as the European E-PROFILE program (Cimini et al., 2020). Some ALCs exhibit a 'blind zone' at low ranges due to imperfect optical overlap between the laser and telescope. However, modern instruments can reach full overlap with proper set-up of the internal optics (Kotthaus and Grimmond, 2018). The effects of imperfect overlap on β can be corrected using a manufacturer algorithm (Lufft, 2016), or as a preprocessing step within PBLH algorithms such as STRATfinder (see section 4.1.2 and Hervo et al., 2016). The ALC used in the field campaign has a wavelength of 1064 nm (Lufft, 2016).

3.3 Data Availability

The MWR and ALC were installed at the field site in January 2022 and have been running almost continuously since (figure 4). The first day on which data is available for both the MWR and the ALC is the 27th of January 2022 and this was chosen as the start of the dataset. A total of 69 eligible (see section 3.2.2) UAV profiles were analysed: 38 in the 2021–22 field season and 31 in the 2022–23 season. 26 RS profiles were analysed: 12 in the 2021–22 field season and 14 in the 2022–23 season. All RS and UAV profiles were taken in connection to cloud seeding experiments, apart from 3 UAV profiles and 5 RS profiles on the 3rd of February 2023, when the profiles were taken specifically for this project (section 5.1). The MWR and ALC datasets were extended beyond one year to include this date.

Due to the low frequency of in situ measurements, the field site does not meet the recommendations of Seibert et al. (2000) for sites intended for systematic comparison of PBLH detection methods. The fact that the UAV and RS ascents are linked to cloud seeding experiments, for which specific conditions are required (section 3.1), imposes a bias on the PBL conditions sampled by these profiles. In particular, the cloudy and cold conditions required for cloud seeding experiments lead to a PBL for which PBLH methods typically show lower agreement. However, this bias is beneficial for the CLOUDLAB project, since instrument performance during an IOP is key.

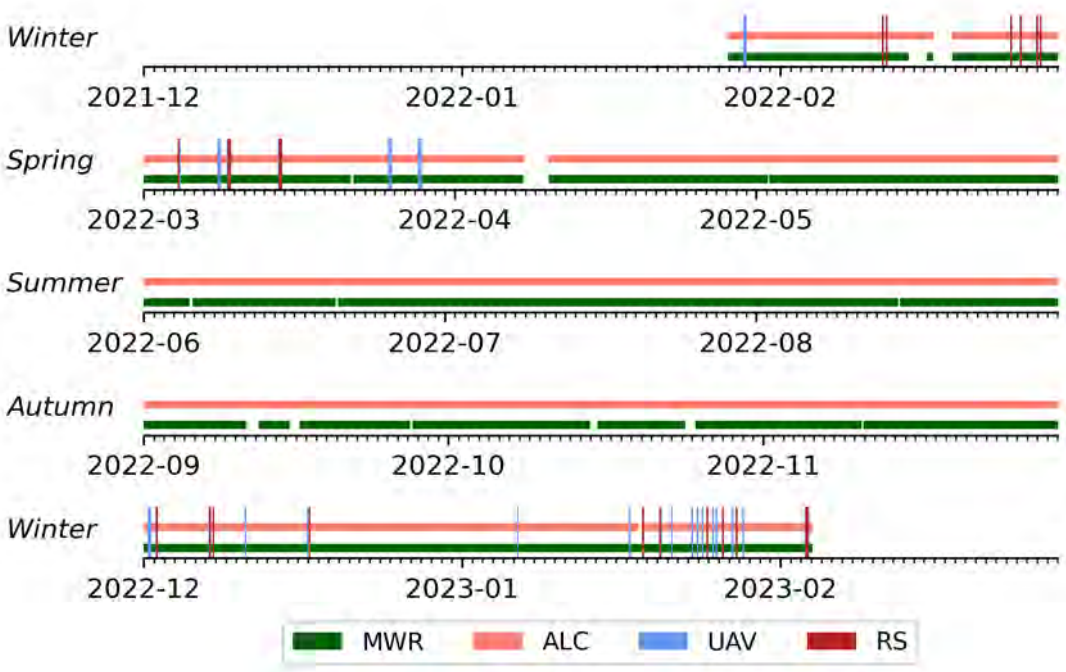

Figure 4: Data availability for the project. The MWR and ALC are running continuously over the whole year, whereas RS and UAVs are mainly flown for cloud seeding experiments in the winter field campaign.

4 Methods: Implementation

4.1 Backscatter Profile Methods

4.1.1 Ceilometer Manufacturer Algorithm

The ALC manufacturer algorithm returns up to three PBLHs at each time point, depending on the number of aerosol layers detected. However, only the lowest PBLH was investigated (referred to as ALC/PBLH). The PBLH is accompanied by a quality score, which is investigated in section 5.2.1. Since the algorithm for the quality score is proprietary and unknown, its assessment is a purely qualitative investigation into the manufacturer's own confidence in the PBLH detection. The algorithm also returns cloud base heights. The lowest cloud base height (CBH) was used to mask for cloudy conditions (section 4.3).

4.1.2 STRATfinder Algorithm

For this project, STRATfinder version 2022c (`https://gitlab.in2p3.fr/ipsl/sirta/mld/stratfinder/stratfinder`) was used. It requires data to be in the E-PROFILE netCDF format instead of the manufacturer's netCDF format. Conversion between the two was done via raw2l1 (`https://gitlab.in2p3.fr/ipsl/sirta/raw2l1`). Configuration parameters for Eriswil are given in appendix B.5. STRATfinder returns an MLH and a PBLH every minute.

STRATfinder includes a temperature-dependent overlap correction function applied in addition to the ALC manufacturer overlap correction (Hervo et al., 2016). This additional correction is instrument-specific and has been shown to reduce backscatter artefacts close to the ground. For the ALC at Eriswil, the relatively stable temperature mean that the correction should not have a 'large impact' on the backscatter (Maxime Hervo, personal correspondence). However, the impact of the overlap correction function on the backscatter or the resulting PBLH was not evaluated systematically for the ALC at the field site.

4.2 Thermodynamic Profile Methods

The thermodynamic profile methods were implemented on RS, UAV and MWR profiles using Python. To reduce computational demands, the PBLH calculations were run on every tenth MWR profile, giving a PBLH approximately every 20 minutes. For methods requiring a vertical gradient, a Savitzky–Golay filter was used for RS and UAV profiles. A Savitzky–Golay filter fits successive subsets of adjacent data points (within a 'window size') with a low degree polynomial using linear least squares. The gradient at each point is then assigned as the gradient of the polynomial fit at that point. The impact of changing the window size and polynomial order were investigated on a case study basis (appendix B.4). Following these investigations, a polynomial order of 3 and window size of 15 were chosen for RS profiles (corresponding to a physical window size of 300 m) whilst a window size of 61 was used for the UAV profiles (corresponding to a physical window size of 305 m). An equal physical window size for the UAV and RS profiles was not possible, as the window size must be odd. For the MWR, the smooth profiles mean that additional smoothing is not appropriate, so vertical gradients were calculated using second order centred differences. For all the thermodynamic methods apart from the SBL methods (section 4.2.6), the search interval for the PBLH was set to 1200 m to 4000 m ASL (280 m to 3080 m AGL). Where no height met the required conditions for a particular method, no value was assigned for the respective PBLH. The thermodynamic PBLH methods are summarised in table 3.

In this project, I did not quantify the uncertainty of the PBLH estimated by each thermodynamic method. This is justified in hindsight by the large differences between the PBLH estimations by different methods applied at the same time, which are expected to be larger than the uncertainty associated with a single method. Uncertainties in the detected PBLH could be assessed firstly by the height resolution of the instruments (for example, the resolution of the MWR at 2000 m AGL is 90 m, see figure 22), by the sensitivity to absolute thresholds defining the PBLH, by the full or half width of the peak used to detect the PBLH or by the accuracy of the measured profiles to which the methods are applied (Heutte, 2021; Seidel et al., 2010).

4.2.1 Elevated Temperature Inversion Method

In the elevated inversion method (EI), the PBLH was detected as the height where the T gradient changed sign from negative to positive (figure 5). Linear interpolation was used to find the likely height of the crossing point between the returned height levels. In the example in figure 5, no PBLH is identified for the MWR temperature profile, as it is too smooth for the gradient to cross zero.

4.2.2 Relative Humidity Gradient Method

For the relative humidity gradient method (RH), the PBLH was taken as the height of the minimum of the vertical gradient of relative humidity (figure 6). A requirement that this minimum had to be a local peak prevented the edge of the search regions being detected as the PBLH.

4.2.3 Potential Temperature Gradient Method

For the potential temperature gradient method (Θ), the potential temperature was first calculated according to equation 1. The value of $\kappa = R_d/c_p$ was taken as 0.286. For the MWR profiles, the pressure was calculated from the temperature profile by assuming hydro-static balance (appendix B.1). The pressure measured by the MWR surface weather station at the nearest available time was taken as p_0 for all profiles. This was chosen such that at the surface, the potential temperature is equal to the temperature: $\theta_0 = T_0$. The PBLH was then taken as the height of the largest local peak in the vertical gradient of θ (figure 7).

4.2.4 Parcel Method

For the parcel method (PM), the PBLH was taken as the height at which the calculated θ profile crosses the surface θ_0 (measured by the surface weather station) from below, including linear interpolation between profile heights (figure 8). If θ at the bottom of the search interval was already greater than θ_0 (as would be the case for a stable PBL), then no PBLH was detected.

4.2.5 Richardson Number Method

The Richardson number was calculated from the UAV and RS profiles according to equation 10, with $\overline{\theta}$ taken as the mean potential temperature up to and including the calculation height, and with the surface wind speeds set to zero to ensure compatibility with COSMO (Collaud Coen et al., 2014). The method was not implemented for the MWR profiles due to a lack of wind measurements. A threshold of 0.25 was initially trialled for PBLH detection for the UAV and RS profiles. However, this threshold was frequently exceeded at ground level due to the stable conditions. In other cases, the PBLH returned showed little relation to the other thermodynamic methods. The Richardson method was therefore not evaluated further in this project.

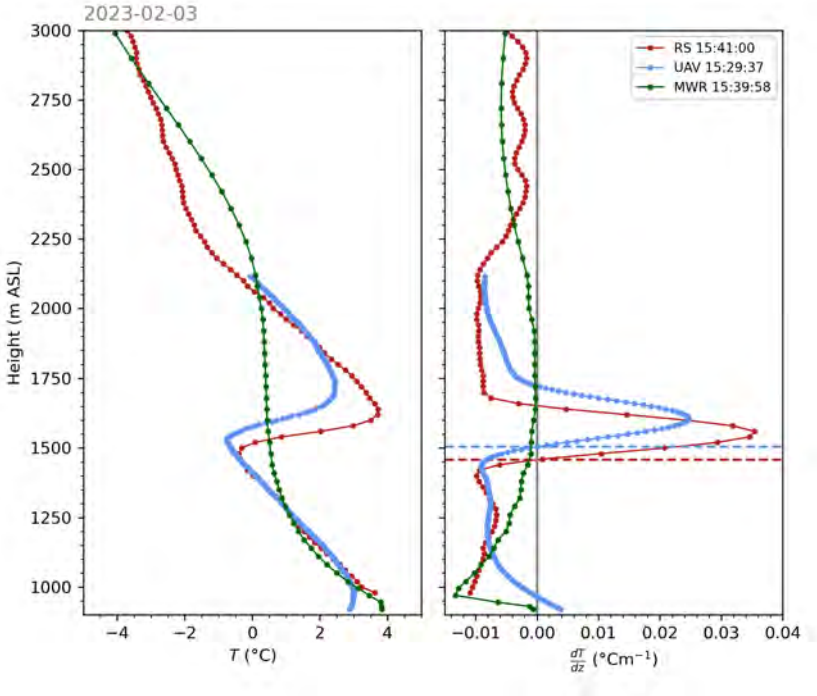

Figure 5: Example of the EI method for profiles taken on the 3$^{\text{rd}}$ of February 2023. The PBLH (dashed horizontal line) is identified where the vertical temperature gradient $\frac{dT}{dz}$ changes sign from negative to positive.

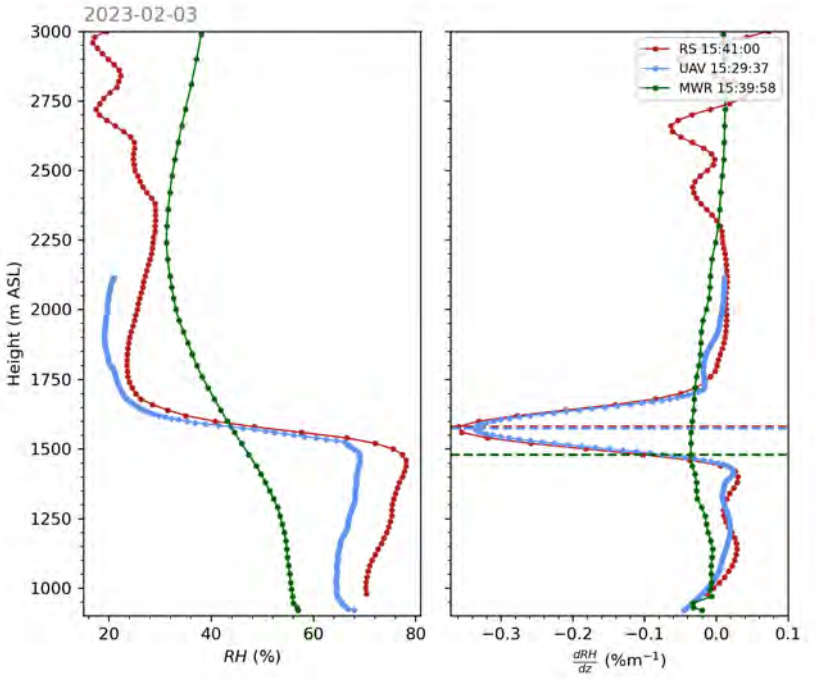

Figure 6: Implementation of the RH method. The PBLH (dashed horizontal line) is identified where the vertical relative humidity gradient $\frac{dRH}{dz}$ shows the largest negative-pointing peak.

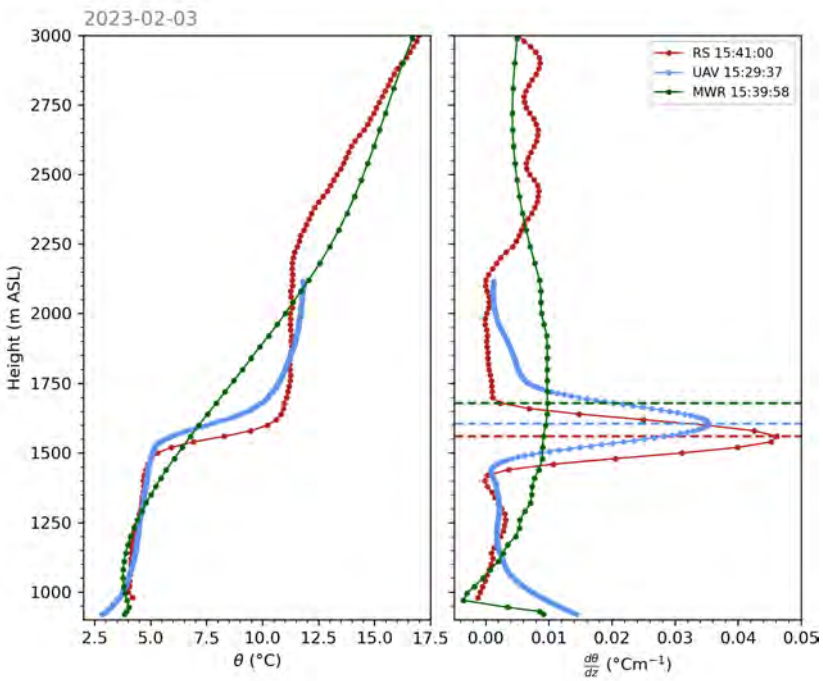

Figure 7: Implementation of the Θ method. The PBLH (dashed horizontal line) is taken as the height where the vertical potential temperature gradient $\frac{d\theta}{dz}$ shows the largest positive-pointing peak.

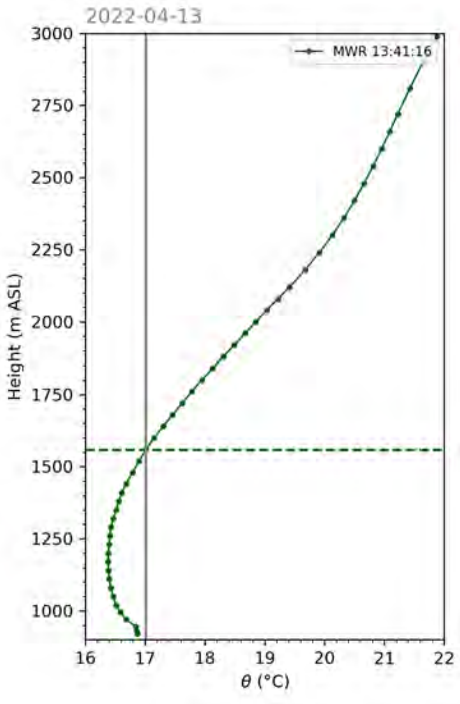

Figure 8: Implementation example of the PM for the 13$^{\text{th}}$ of April 2022. The PBLH (dashed horizontal line) is identified where the potential temperature is equal to the potential temperature measured by the surface weather station (vertical grey line).

4.2.6 Nocturnal Surface Boundary Layer Detection

The SBI height was taken as the first height at which the temperature gradient changed sign from positive to negative, including linear interpolation between profile heights (figure 9). This therefore detects the *top* of the SBI, whereas the EI method (section 4.2.1) detects the *base* of the elevated inversion. The SBL was also detected from θ (SBLpT method), as the height of the first (lowest height) local minimum in the vertical gradient of θ which had a peak value smaller than 0.003 $^{\circ}\mathrm{Cm}^{-1}$ (figure 10). This threshold is intermediate between those of Li et al. (2021) and Heutte (2021) and was chosen after visual inspection of a range of profiles. For both SBL methods, the search region was set to between 950 m ASL and 2000 m ASL to reflect the lower expected height of the SBL. The lower search region threshold was still set above the ground level to avoid artefacts close to ground (discussed in appendix B.4).

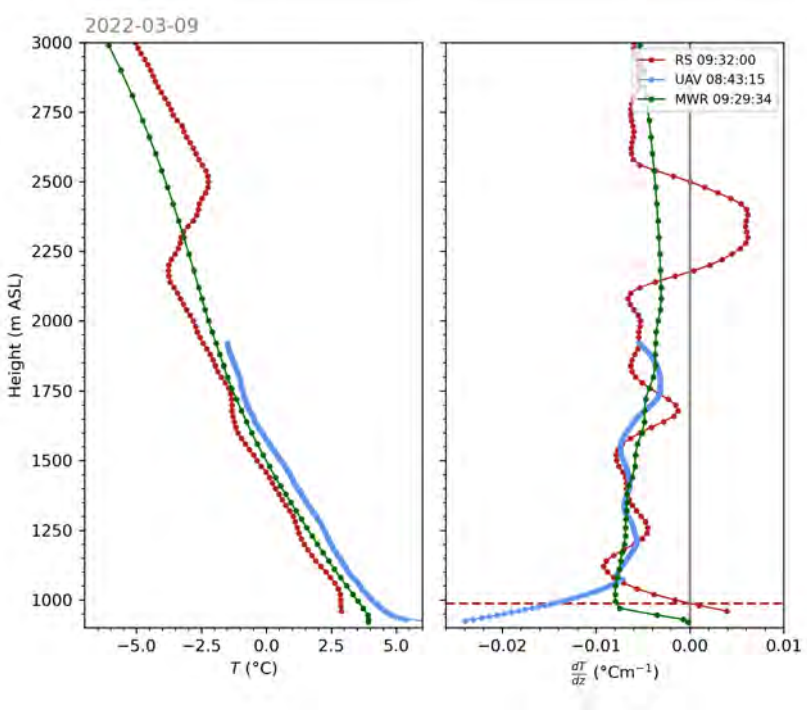

Figure 9: Implementation of the SBI method for profiles taken on the 9$^{\text{th}}$ of March 2022. An SBI (dashed horizontal line) is taken as the height where the vertical temperature changes sign from negative to positive. In this example, an SBI is only detected by the RS profile.

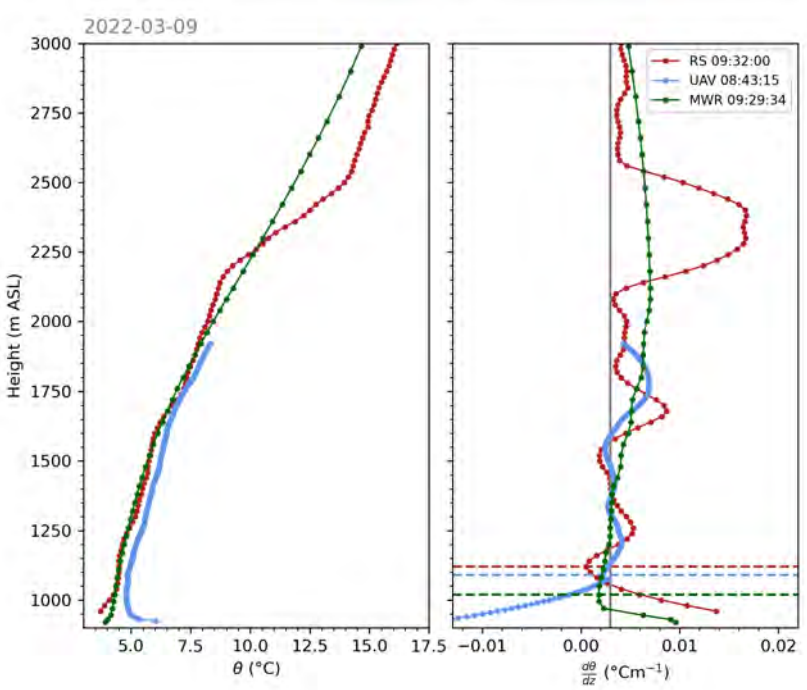

Figure 10: Implementation of the SBLpT method for profiles taken on the 9$^{\text{th}}$ of March 2022. The SBL top (dashed horizontal line) is identified as the lowest height at which the vertical potential temperature gradient $\frac{d\theta}{dz}$ has a local negative-pointing peak with a peak value smaller than 0.003 °Cm^{-1} (vertical grey line).

Acronym	**Method**	**Criteria**
EI	Elevated Temperature Inversion	First height above 1200 m ASL at which the temperature gradient crosses zero from below
RH	Relative Humidity Gradient	Height of the largest negative-pointing peak in the relative humidity gradient between 1200 m and 4000 m ASL
Θ	Potential Temperature Gradient	Height of the largest positive-pointing peak in the potential temperature gradient between 1200 m and 4000 m ASL
PM	Parcel Method	First height above 1200 m ASL at which the measured potential temperature crosses the surface potential temperature from below
SBI	Surface-based Inversion	First height above 950 m ASL at which the temperature gradient crosses zero from above
SBLpT	Surface Boundary Layer Detected by the Potential Temperature Gradient	First height above 950 m ASL at which the potential temperature gradient has a negative-pointing local peak with peak value less than 0.003 °Cm^{-1}

Table 3: Thermodynamic PBLH methods implemented and evaluated in this study. Note that the field site is at 920 m ASL.

4.3 Method and Instrument Comparisons

Since there is no universal standard for the PBLH, several instrument-method comparisons were made. For the ALC, the manufacturer algorithm was compared to STRAT/MLH and STRAT/PBLH. The PBLH estimated from UAV, RS, and MWR profiles were compared for each thermodynmaic method in turn. Since RS profiles are often used as a standard for PBLH detection, both the MWR and UAVs were compared to the RS. The remaining comparison between the UAVs and MWR is given in appendix C.1. To compare thermodynamic and aerosol PBLH indicators, the thermodynamic methods were compared to STRAT/PBLH and STRAT/MLH. STRATfinder was chosen over the ALC manufacturer algorithm for this comparison due to its open-source nature. The methods RH, θ, EI and PM were compared to STRAT/PBLH, since these are expected to signal the top of the CBL in the day and RL at night. However, comparisons to the STRAT/MLH were also made. The SBI and SBLpT were compared to STRAT/MLH.

For each comparison, the following metrics were used to assess the agreement: number of samples under comparison (N), slope (a) and intercept (b) of a linear regression fit, the coefficient of determination between the data and the linear fit (R^2), the coefficient of determination between the data and 1:1 line (R^2_{one}), the mean absolute error (MAE), the median of the difference between the two methods (M_Δ), and the proportion of samples for which the two methods agree to within 250 m (P_{250}) or 100 m for the SBI and SBLpT methods (P_{100}). Often, a linear fit is fairly unrepresentative of the observations. For comparisons of methods implemented on the MWR or ALC data, the number of observation points is set by the instrument or method with the lowest temporal resolution (table 2). Comparisons are then made with the closest time points of the second instrument or method. For the comparison of RS and UAVs, profiles are only compared if the difference in flight start times is less than 90 minutes (chosen as a compromise between the desire to only compare profiles close in time and still have sufficient profiles to compare, section 5.3.1). The definitions of the statistical metrics are given in appendix B.6.

In contrast to previous studies, instrument and method comparisons were first made without post-processing, in order to assess the consistency of the different methods over all atmospheric conditions. To investigate method performance in different stages of the diurnal PBL cycle, comparisons were split by the time of day relative to sunrise and sunset (table 4). These times of day are the same as those used in the initial evaluation of STRATfinder by Kotthaus et al. (2020). The Python package 'SunTime' was used to find the sunrise and sunset times. To assess the performance under cloud-free conditions, all times with a cloud base height lower than 5000 m ASL were removed. This filter was motivated not by the desire to investigate only cloud-free *days*, when the PBLH evolution is likely to adhere better to the ideal behaviour described in section 1.2.1, but rather to remove the possibility of false attribution of the PBLH to the cloud base or top. Time points with precipitation were not explicitly removed, but are expected to be largely removed by the cloud filter. A summary of all statistical comparisons is given in table 5. Further investigations of instrument and method performance under different atmospheric conditions were made with case study days (section 5.1).

Time of Day	**Time Window**
Morning (MO)	sunrise until sunrise +4 h
Daytime (DT)	sunrise +4 h until sunset −2 h
Evening (EV)	sunset −2 h until sunset +2 h
Night-Time (NT)	sunset +2 h until sunrise

Table 4: Definitions of the times of day used for PBLH method comparisons (h = hour).

Comparison		**Table**	**Figure**	**Time of Day**	**Removing Clouds**
x	y				
ALC/PBLH	STRAT/PBLH	6	13	✓	✓figure 26
ALC/PBLH	STRAT/MLH	7	14	✓	✓figure 27
RS/EI	UAV/EI	8	15	✗	✗
RS/RH	UAV/RH	8	15	✗	✗
RS/Θ	UAV/Θ	8	15	✗	✗
RS/SBLpT	UAV/SBLpT	8	16	✓	✗
RS/EI	MWR/EI	9	17	✗	✗
RS/RH	MWR/RH	9	17	✗	✗
RS/Θ	MWR/Θ	9	17	✗	✗
RS/SBLpT	MWR/SBLpT	9	18	✓	✗
MWR/EI	UAV/EI	14	24	✗	✗
MWR/RH	UAV/RH	14	24	✗	✗
MWR/Θ	UAV/Θ	14	24	✗	✗
MWR/SBLpT	UAV/SBLpT	14	25	✓	✗
STRAT/PBLH	MWR/EI	10	19	✓	✓figure 28
STRAT/PBLH	MWR/RH	10	19	✓	✓figure 28
STRAT/PBLH	MWR/Θ	10	19	✓	✓figure 28
STRAT/PBLH	MWR/PM	10	19	✓	✓figure 28
STRAT/MLH	MWR/EI	11	19	✓	✓figure 28
STRAT/MLH	MWR/RH	11	19	✓	✓figure 28
STRAT/MLH	MWR/Θ	11	19	✓	✓figure 28
STRAT/MLH	MWR/PM	11	19	✓	✓figure 28
STRAT/MLH	MWR/SBI	12	20	✓	✓figure 29
STRAT/MLH	MWR/SBLpT	12	20	✓	✓figure 29

Table 5: Method and instrument comparisons in this project. 'Time of Day' indicates whether comparisons were made split by the time of day relative to sunrise (table 4). 'Removing Clouds' indicates whether additional comparsions were made when all time points with cloud bases below 5000 m were removed. All comparisons are given in the form instrument/method, apart from those referring to the MLH and PBLH from STRATfinder.

5 Results and Discussion

5.1 Case Study Days

Figure 12 shows three case study days for PBLH detection at the CLOUDLAB field site. Figure 12a shows a day with PBLH evolution closely matching the textbook evolution described in section 1.2.1. In the dataset of just more than a year, there were fewer than 5 days for which the tracked layers corresponded closely to the ideal daily evolution. These all occurred outside the winter field campaigns, so there are no UAV or RS profiles. The daytime CBL starts to grows from 1100 m ASL at 08:00 UTC to 2100 m ASL at 16:00 UTC and is tracked by both ALC/PBLH and STRAT/MLH. From 00:00 to 06:00 UTC, both the RL (tracked by STRAT/PBLH) and the SBL (tracked by ALC/PBLH and STRAT/MLH) can be seen. For the thermodynamic methods, the Θ method appears to track the PBLH well, specifically tracking the RL at night. The RH method also tracks the daytime PBLH, though at night it gives an intermediate height between that of the SBL and the RL. The PM can only be applied to three profiles during growth of the CBL. This indicates that the PBL is only unstable with respect to vertical mixing from the surface during this growth phase. When the PM is successful, the detected height underestimates the PBLH compared to other methods. This disagrees with the results of Kotthaus et al. (2020), who found that STRAT/MLH was typically smaller than the PBLH estimated by the PM during the growth phase. The criteria for the SBLpT method (section 4.2.6) are met during the day and evening but not at night, in contrast to the expected nocturnal SBL. For the one profile for which an SBI is detected, this lies below the height detected by the SBLpT method as expected.

Figure 12a also highlights that the time of day divisions used by Kotthaus et al. (2020) (table 4) may not be ideally suited to the PBLH evolution at Eriswil. The MLH growth is not constrained to the MO period, but continues over the DT period and even into the EV period. Due to the low number of such 'ideal' days, it was not possible to establish whether this delayed and extended growth stage was a consistent feature of the PBL at Eriswil. The method comparisons split by the time of day (section 5.2.2 and 5.3.3) are likely to show smaller differences in agreement than they would do if the time of day divisions perfectly matched distinct stages of PBL evolution.

For the case study day on the 3$^{\text{rd}}$ of February 2023 (figure 12b), no such clear diurnal evolution can be seen. On this day, RS and UAV profiles were taken specifically for PBLH measurements, rather than in connection with cloud seeding experiments. Despite the lack of a clear growth phase, the PBL does have a distinct top, defined by an EI and strong θ, RH and backscatter gradients. For the UAV and RS profiles, the marker for the Θ method is covered by that for the RH method. The agreement between the EI, Θ, RH and aerosol backscatter methods is generally good. The PBLH is also low enough that all of the UAV profiles go high enough to detect it. An SBI is detected by the UAV profiles in the afternoon but not by the closest RS profiles or by the MWR. The criteria for the SBLpT method are met during most of the day, and the SBL height returned is noticeably higher for the RS and UAV profiles than for the MWR. It is therefore unclear whether a stable SBL is truly present for the entire day, or whether the criteria for the SBLpT method lead to the detection of artefacts in the MWR profiles close to the ground. Finally, the presence of clouds after 22:00 UTC leads to ALC/PBLH detecting a height above the CBH. This is assumed to be the cloud top, where a strong decrease in the backscatter with increasing height leads to a similar backscatter signal to that at the PBLH.

The same phenomenon is observed on the 25$^{\text{th}}$ of February 2022 (figure 12c), which serves

as a case study for the interplay of clouds and the PBLH. Whereas ALC/PBLH follows the variation of the CBH relatively consistently, STRAT/PBLH and STRAT/MLH sometimes follow the clouds (such as STRAT/PBLH after 23:00 UTC) but often do not (such as between 17:00 UTC and 19:00 UTC). On this day the thermodynamic methods show poor agreement with the aerosol methods. Particularly the Θ and RH methods give a PBLH which stays almost constant throughout the day, whereas the aerosol methods show fast changes. At two time points the PM is successful, but the detected MLH is around 300 m below that detected by the aerosol methods. This case study also serves to illustrate the issue of UAV profiles not going high enough to detect the PBLH: the three UAV profiles before midnight all have maximum heights lower than 1800 m ASL and are hence unable to detect the same features in the Θ and RH methods as are detected in the RS profile. This is discussed further in section 5.3.1.

5.2 Backscatter Profile Methods

5.2.1 Manufacturer Algorithm

The manufacturer algorithm returned a PBLH at 42% of the time points at which the ALC returned backscatter data. According to the quality flag, fewer than 0.01% of the missing time points were due to a lack of raw data for calculation or a system hardware failure. 0.03% were due to the algorithm not being able to generate a value. The vast majority corresponded to time points when none of the above errors occurred but no PBLH was detected by the algorithm (Lufft, 2016). Figure 11 shows the distribution of missing PBLH by month, including the manufacturer quality flag when the PBLH is detected. As discussed in section 4.1.1, the criteria for the quality flag are unknown. December is the month with the highest proportion of missing PBLH. This may be due to multiple days with fog, leading to high backscatter close to the ground and very low backscatter above. The detected PBLH in autumn and winter are assessed as having a lower quality than those in spring and summer. This is likely due to the increased occurrence of low-level clouds and less distinct backscatter changes at the PBLH in winter.

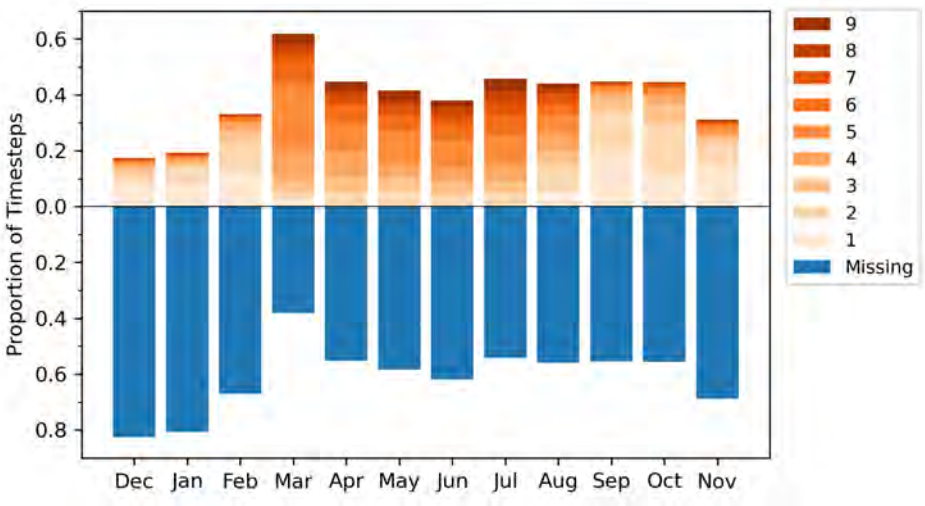

Figure 11: Manufacturer quality flag for the ALC manufacturer algorithm PBLH. The quality flag for non-missing time points goes from 1 (layer can be detected but with high uncertainty and low accuracy) to 9 (layer can be detected with a high accuracy, less than 50 m - Lufft, 2016) The algorithm used for assigning the quality flag is unknown. The bars for January and February include data from both 2022 and 2023 (see figure 4)

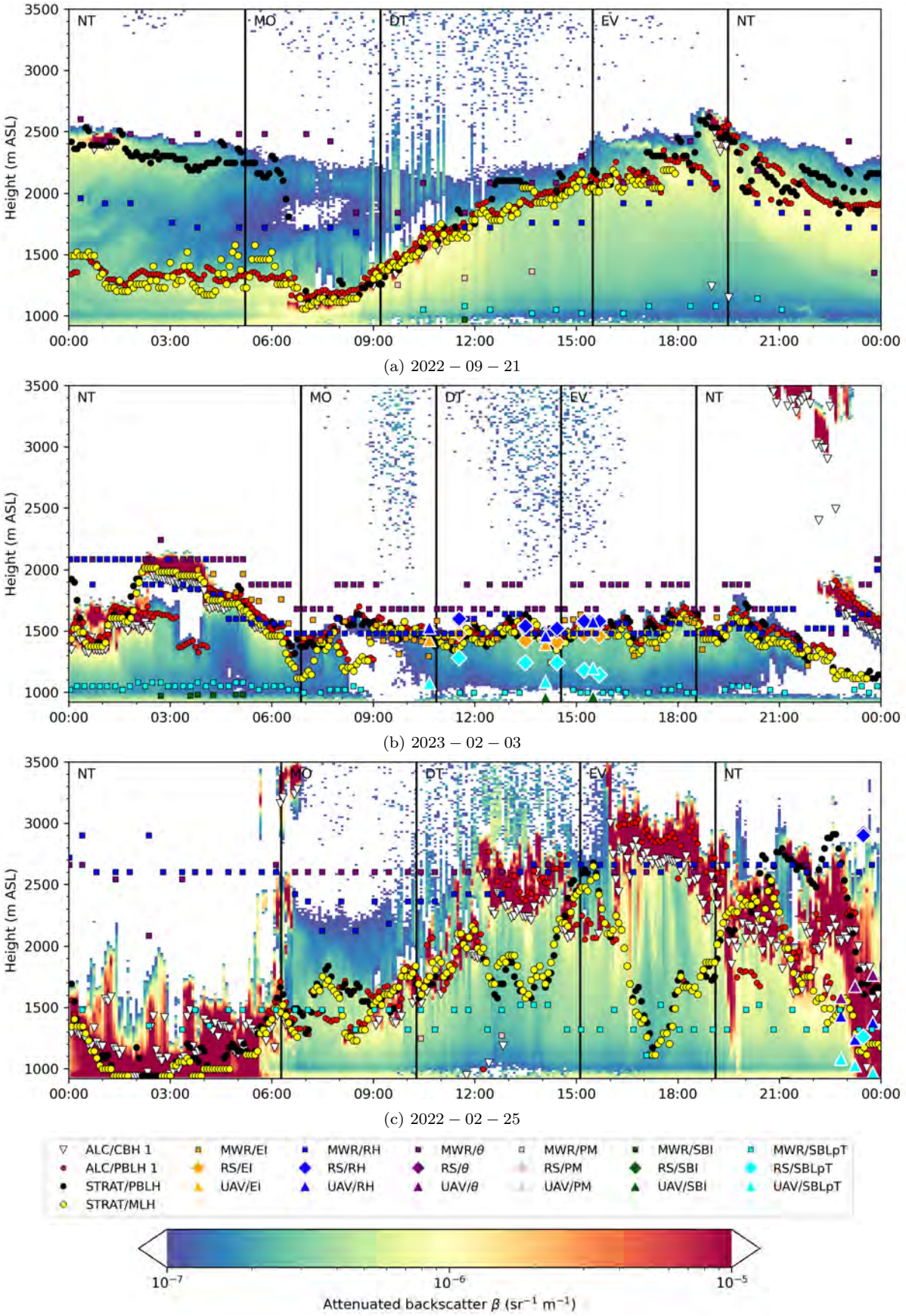

(a) 2022 – 09 – 21

(b) 2023 – 02 – 03

(c) 2022 – 02 – 25

Figure 12: Case study days for PBLH investigation. The background backscatter, manufacturer PBLH and CBH and STRATfinder layers are resampled (using the median) to 5 minute intervals for plotting. All times are in UTC. Black vertical lines indicate the divisions between the times of day relative to sunrise, as defined in table 4. Backscatter larger than 10^{-5} $\mathrm{sr}^{-1}\mathrm{m}^{-1}$ or smaller than 10^{-7} $\mathrm{sr}^{-1}\mathrm{m}^{-1}$ is shown in white.

5.2.2 STRATfinder Algorithm

Figure 13 shows STRAT/PBLH against ALC/PBLH, split by the time relative to sunrise (table 4). The statistical results for this comparison are shown in table 6. The corresponding results for the comparison with STRATfinder MLH are given in figure 14 and table 7.

Although there is a higher concentration of points in the vicinity of the 1:1 line, it is evident that there are many time points when the two methods do not agree. The high concentration of points above the 1:1 line and negative M_Δ indicates that in general, STRATfinder PBLH is equal or higher than the PBLH from the ALC algorithm. Overall, no large changes in agreement are seen for the different times of day. Case study analysis (section 5.1) revealed that when an 'ideal' daily evolution in observed, ALC/PBLH detects the SBL top rather than RL top and is therefore expected to show better agreement with STRAT/MLH than STRAT/PBLH during the night. However, only a small increase in the number of points above the 1:1 line is observed at night compared to other periods in the day.

The comparison between ALC/PBLH and STRAT/MLH (figure 14) reveals a more symmetric distribution at all times of day, with no large differences between the number of points above and below the 1:1 line. The P_{250} is also greater and MAE smaller for all times of day compared to the STRAT/PBLH comparison. This supports the hypothesis that ALC/PBLH detects the SBL top rather than RL top at night and hence is a better indicator of the MLH than the PBLH.

Removing time points with cloud bases lower than 5000 m ASL (see figures 26 and 27 in appendix C.2) does not result in a consistent improvement in agreement between the ALC/PBLH and either STRAT/PBLH or STRAT/MLH: although P_{250} increases slightly in the DT period, it decreases during the NT period. A decrease in agreement when clouds are removed is not unexpected, since the presence of clouds within the PBL can lead to both methods detecting the cloud boundary as the PBLH (see examples in section 5.1). In these cases, the two methods will agree with each other even if the assigned PBLH is not consistent with that from thermodynamic methods. For the comparison to STRAT/PBLH, removing clouds does not result in a convincing decrease in the number of points above the 1:1 line, so these points cannot be explained by false attribution of the PBLH to cloud layers.

	Without Processing					Removing Clouds				
	All	MO	DT	EV	NT	All	MO	DT	EV	NT
N_t	972017	162045	295407	161850	352715	491088	81628	152710	85992	170758
N	772622	124509	235432	129075	283606	490751	81529	152680	85942	170600
P_{250} (%)	46.4	41.2	52.4	51.2	41.5	46.2	39.8	54.3	51.9	39.1
a	0.55	0.50	0.58	0.61	0.53	0.52	0.51	0.62	0.57	0.47
b (m)	1305	1428	1175	1138	1394	1392	1468	1121	1250	1545
R^2	0.15	0.11	0.16	0.20	0.14	0.12	0.09	0.15	0.15	0.11
R^2_{one}	-0.23	-0.36	-0.14	-0.08	-0.29	-0.32	-0.46	-0.17	-0.19	-0.43
M_Δ (m)	194	310	50	93	281.7	238	368	64	93	353
MAE (m)	619	701	539	541	685	633	725	527	547	727

Table 6: Statistical results for STRAT/PBLH (y) and ALC/PBLH (x). N_t gives the total number of time points at which the ALC returns data in each time period relative to sunrise (table 4). Definitions of statistical metrics are given in appendix B.6.

	Without Processing					Removing Clouds				
	All	MO	DT	EV	NT	All	MO	DT	EV	NT
N_t	972017	162045	295407	161850	352715	491088	81628	152710	85992	170758
N	580197	77520	215604	62639	183730	357379	47839	138464	66119	104957
P_{250} (%)	67.2	72.4	69.9	60.6	65.7	70.0	72.3	73.0	62.8	69.5
a	0.44	0.21	0.52	0.41	0.21	0.51	0.12	0.64	0.42	0.20
b (m)	885	1101	882	1027	1100	775	1202	658	1037	1120
R^2	0.21	0.08	0.27	0.15	0.09	0.23	0.02	0.35	0.13	0.07
R^2_{one}	-0.20	-1.37	0.03	-0.20	-1.47	-0.01	-1.72	0.25	-0.12	-1.46
M_Δ (m)	-66	-67	-37	-52	-80	52	-67	-37	-52	-67
MAE (m)	303	247	285	364	312	269	233	244	339	275

Table 7: Statistical results for STRAT/MLH (y) and ALC/PBLH (x). N_t gives the total number of time points at which the ALC returns data in each time period relative to sunrise (table 4).

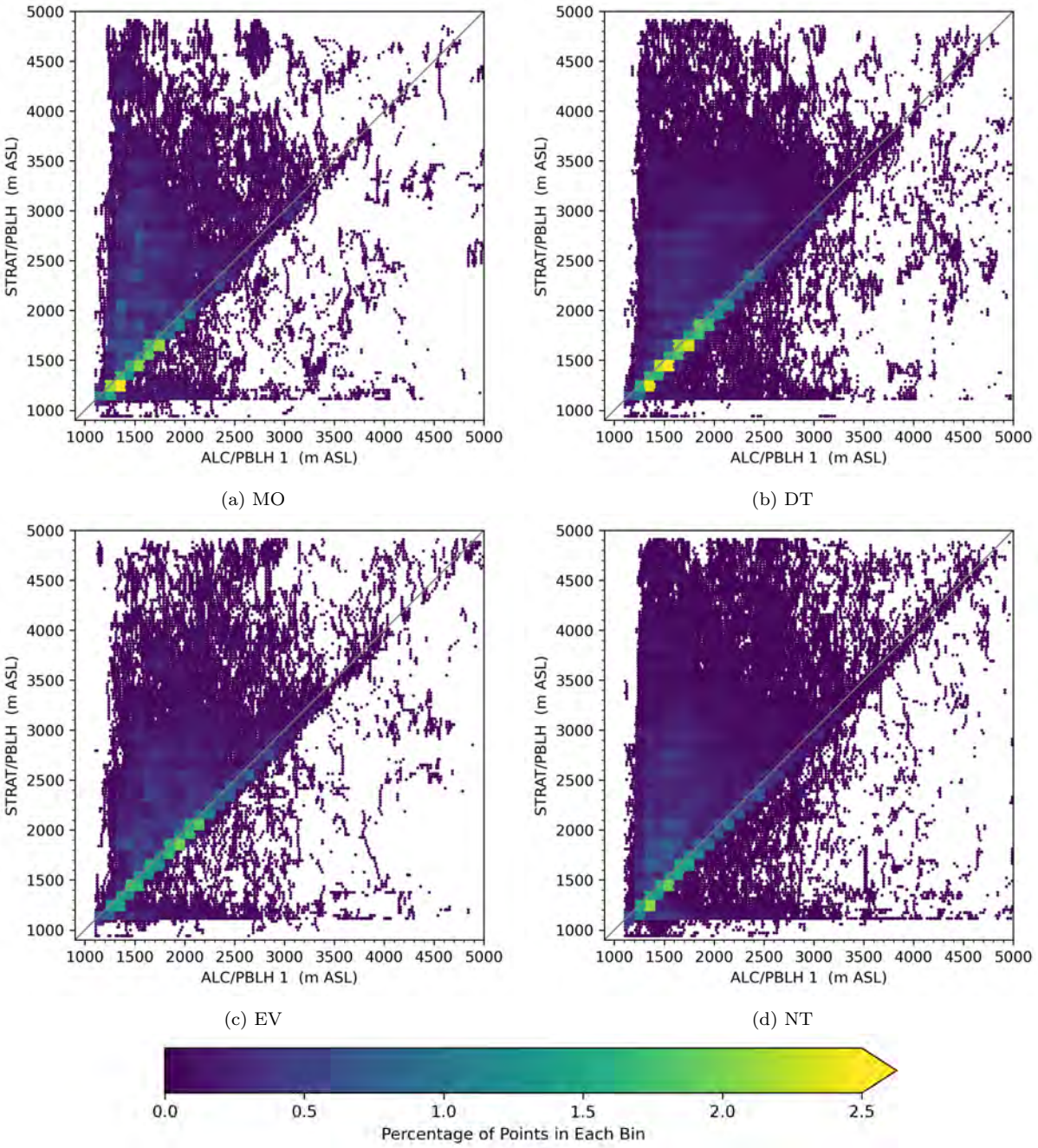

(a) MO

(b) DT

(c) EV

(d) NT

Figure 13: Comparison of STRAT/PBLH and ALC/PBLH (called ALC/PBLH 1 in this figure) for times relative to sunrise, defined in table 4. Points are coloured according to the percentage of the points in each time division that lie within each 100 m by 100 m bin. The grey line indicates the 1:1 line.

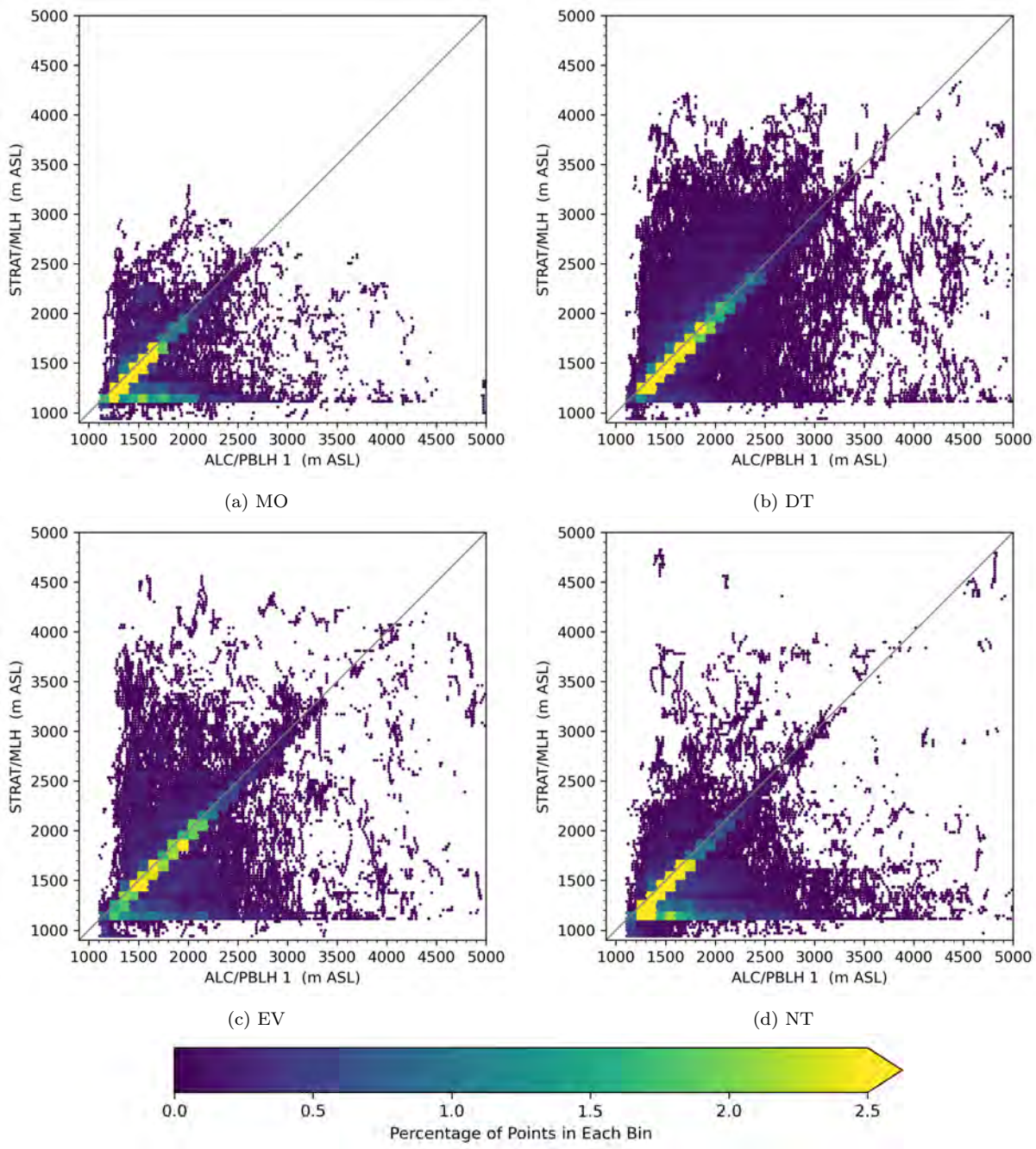

(a) MO

(b) DT

(c) EV

(d) NT

Figure 14: Comparison of STRAT/MLH and ALC/PBLH for the times defined in table 4. Points are coloured according to the percentage of the points in each time division that lie within each 100 m by 100 m bin. The grey line indicates the 1:1 line.

5.3 Thermodynamic Methods

5.3.1 Instrument Comparison: Radiosondes and Unmanned Aerial Vehicles

A total of 16 RS profiles were paired to UAV profiles with a start time within 90 minutes. The number of profiles in the times of day MO, DT, EV and NT was four, five, one and six respectively. Nine profiles were taken at times when the CBH detected by the ALC was lower than 5000 m ASL. None of the profiles were taken at times with precipitation according to the rain flag of the surface weather station. Figure 15 shows the comparison of UAVs and RS for the three methods EI, RH and Θ. The PM and Richardson number methods could not be used for any of the paired profiles, due to the stable conditions. There were also no paired profiles for which an SBI was detected in both the UAV and RS profiles. Figure 16 shows the comparison of the SBLpT method. Statistical comparisons between the instruments for each method are given in table 8.

The EI method shows the best agreement between the two instruments, which can be attributed to the strictness of the method: when an elevated inversion is present, it is an unambiguous marker of the PBLH and can be detected by the RS and UAV . In contrast, the RH and Θ methods only require a peak to be present in the gradient of RH and θ respectively. A PBLH is therefore detected for every profile, even when the detected peak is not a concrete signature of the PBLH. This is particularly the case for UAV profiles which don't reach the PBLH, resulting in a large positive bias between the PBLH detected by the RS and UAV in these cases. The agreement between the instruments increases when UAV profiles whose maximum height is below the PBLH detected by the RS are removed. The extent to which the vertical gradient profiles are smoothed before the PBLH methods are applied also has a small influence on the PBLH, as it affects the number and size of the peaks in the gradient profile. This is discussed further in appendix B.4. For the SBLpT method, peaks meeting the required conditions (section 4.2.6) are detected in all periods of day. No clear increase in agreement between the instruments is observed during NT, when a true stable SBL is expected to occur most frequently. For SBL detection, the issue of the UAV profiles not going high enough does not apply. Future application of UAVs for PBL characterisation could therefore focus on high resolution, automated detection of the SBL.

	EI	**RH**	**Θ**	**SBLpT**
N	9	16 (7)	16 (7)	15
P_{250} (%)	88.9	43.8 (85.7)	37.5 (71.4)	33.3
a	1.07	-0.03 (0.60)	-0.10 (-0.03)	0.15
b (m)	-12	1609 (694)	1679 (1572)	951
R^2	0.58	0.00 (0.19)	0.08 (0.00)	0.02
R^2_{one}	0.34	-6.39 (-0.10)	-16.63 (-0.76)	-2.04
M_Δ (m)	-165	-278 (65)	-528 (30)	-145
MAE (m)	102	455 (154)	636 (162)	175

Table 8: Statistical results for thermodynamic PBLH methods implemented on UAV (y) and RS (x) profiles, for the 16 paired profiles with start times within 90 minutes. The numbers in brackets are for comparisons made with only UAV profiles which reach a maximum height greater than the PBLH detected with the RS profile. For the EI and SBLpT methods, this condition was met for all the UAV profiles. The SBLpT method was applied for profiles at all times of day, rather than just nocturnal profiles. Note that for the SBLpT method, the number in the P_{250} row is actually P_{100}.

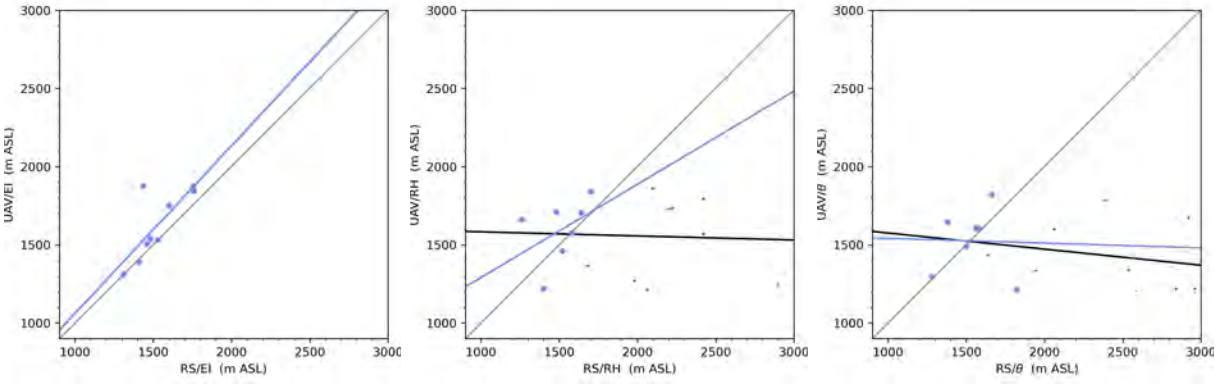

(a) (b) (c)

Figure 15: Comparison of PBLH detected by RS and UAV profiles. Points in blue are those for which the maximum height reached by the UAV is greater than the PBLH detected from the RS profile. The grey line is the 1:1 line. The black and blue lines are linear regressions of all points and blue points only respectively.

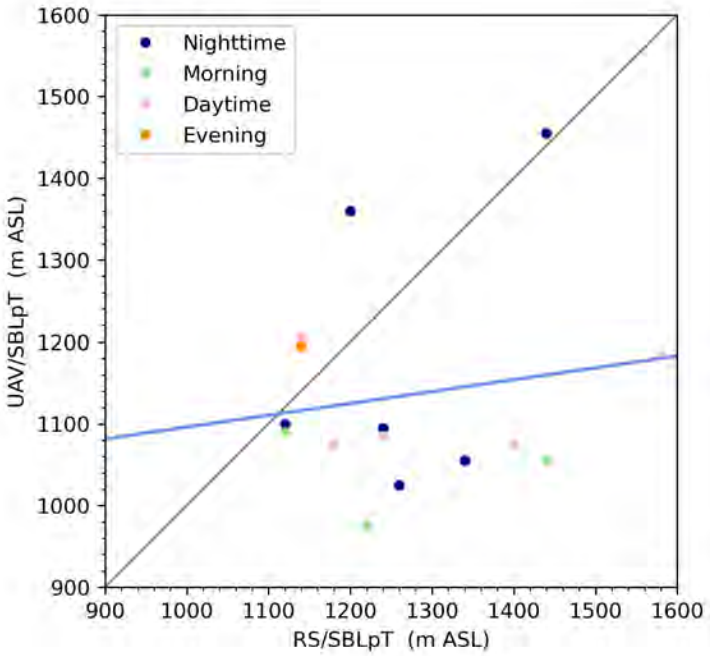

Figure 16: Comparison of RS and UAV profiles for the SBLpT method. The grey line is the 1:1 line. The blue line is the linear regression with all points. Points are coloured according to the time of day relative to sunrise, as defined in table 4.

5.3.2 Instrument Comparison: Radiosondes and Microwave Radiometer

Figures 17 and 18 and table 9 show the inter-instrument comparisons for each method for the MWR and RS profiles. Again, there were no times at which an SBI was detected by both the RS and MWR profiles, nor any RS profiles for which the PM could be used. The smoothness of the MWR temperature profile means that the vertical temperature gradient often does not cross zero when an EI is detected by the RS (this can be seen in the example in figure 5). To counter this, a less strict threshold could be used for EI detection for MWR profiles. However, this would result in a higher number of PBLH detections for profile signatures which may not be a robust indicator of the PBLH. Conversely, *if* an EI is detected by the MWR profile despite the high smoothness and strict zero-crossing requirement, it is likely to be a robust indicator of the PBLH. For the Θ and RH methods, the smooth gradient profiles of the MWR often only show one peak in the search region, which is often not at the same height as the largest peak in the corresponding RS profile. For the SBLpT method, the agreement between the SBL top detected by the RS and MWR is low, and no clear pattern is observed between SBL detections at different times of day. The same comparisons for the MWR and UAV profiles are given in appendix C.1.

	EI	**RH**	Θ	**SBLpT**
N	5	26	26	14
P_{250} (%)	80.0	57.7	58	28.6
a	-1.65	0.45	0.62	-0.08
b (m)	3837	1014	775	1219
R^2	0.33	0.19	0.63	0.00
R^2_{one}	-0.85	-0.10	0.39	-0.58
M_Δ (m)	-38	-70	120	-123
MAE (m)	128	312	247	190

Table 9: Statistical results for thermodynamic PBLH methods implemented on MWR (y) and RS (x) profiles, for the 26 RS profiles. The SBLpT method was applied for profiles at all times of day, rather than just nocturnal profiles. Note that for the SBLpT method, the number in the P_{250} row is actually P_{100}.

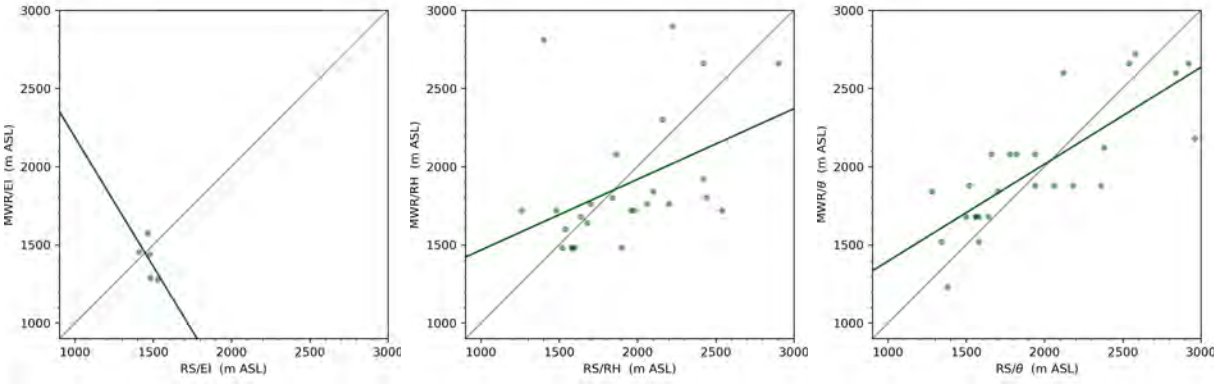

(a) (b) (c)

Figure 17: Comparison of PBLH detected from RS and MWR profiles. The grey line is the 1:1 line. The dark green line shows the linear regression.

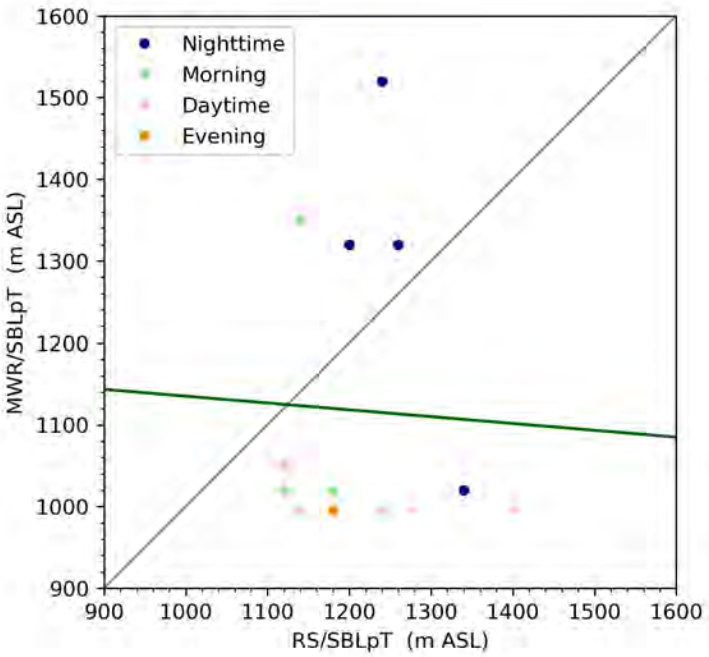

Figure 18: Comparison of RS and MWR for the SBLpT method. The grey line is the 1:1 line. The dark green line is the linear regression with all points. Points are coloured according to the time of day relative to sunrise, as defined in table 4.

5.3.3 Method Comparison to STRATfinder

Figure 19 shows the comparison between the thermodynamic PBLH methods and the PBLH and MLH returned by STRATfinder. The PBLH comparison statistics are given in table 10, whilst the corresponding MLH statistics are given in table 11. On a systematic level, the agreement between the PBLH detected by the thermodynamic methods and STRATfinder is generally poor. For all methods, the negative R^2_{one} indicates that the points would be better described by a horizontal line than a line showing 1:1 agreement (see appendix B.6). An overestimation of the PBLH detected by aerosol methods compared to thermodynamic methods observed by Seibert et al. (2000) was not seen here, with all thermodynamic methods apart from PM having a positive M_Δ compared to STRAT/PBLH. The methods RH and Θ return a PBLH at a high percentage of time points (98% and 99% respectively) but have a low P_{250} and the largest range of differences compared to STRAT/PBLH. No consistent change in agreement between thermodynamic methods and STRAT/PBLH is observed based on the time of day. As discussed in section 5.1, this may be due to the time of day divisions (table 4) not reflecting the typical daily evolution of the PBLH at Eriswil.

For the comparison of the thermodynamic methods to STRAT/MLH, there are slightly fewer comparison points. This is due to the higher number of time points with missing STRAT/MLH compared to STRAT/PBLH. The number of points for which the thermodynamic PBLH is greater than the STRAT/MLH (negative difference in figure 19) is smaller than for STRAT/PBLH. This is expected, since STRATfinder is configured such that the MLH is always less than the PBLH (Kotthaus et al., 2020) and STRAT/MLH is expected to return the SBL top at night. However, the agreement with STRATfinder for the RH and Θ methods does not show large changes between the MLH and PBLH. This means that the hypothesis that the RH and Θ methods are more representative of the RL than the SBL at night cannot be clearly confirmed. For the PM, the agreement to STRAT/MLH is higher than to STRAT/PBLH. This is expected, since the PM by definition should give the height to which air parcels can mix adiabatically from the ground surface.

Comparisons for the SBL detection methods are given in figure 20 and table 12, for STRAT/MLH only. There are more time points meeting the requirement for the SBLpT method than SBI, which is expected as the requirement is less strict (section 4.2.6). Both methods show a small increase in agreement with STRAT/MLH at night. STRAT/MLH is expected to indicate the top of the CBL during the day, so the agreement with a detected SBL is expected to be low.

Removing time points with cloud base heights lower than 5000 m ASL does not result in a consistent improvement of thermodynamic method agreement with either STRAT/PBLH or STRAT/MLH. The figures for these comparisons are given in appendix C.2. The largest change is seen for P_{250} for the EI method, which increases when cloudy time points are removed (from 74.9% to 84.6% in the DT period for STRAT/PBLH). Based on the case study analysis, this is likely due to STRATfinder assigning a cloud boundary as the PBLH, even when an EI is present. In contrast, the agreement between MWR/PM and STRAT/PBLH decreases when cloudy time points are removed. The RH, Θ, SBI and SBLpT methods do not show a clear change in agreement with STRATfinder when cloudy time points are removed. Attempts to characterise the conditions under which the PBLH methods show poor or good agreement more systematically using composite profiles were not successful: since a large variety of conditions lead to disagreement between the methods, averaging over these conditions leads to similar atmospheric profiles for the groups of time points with high and low P_{250}.

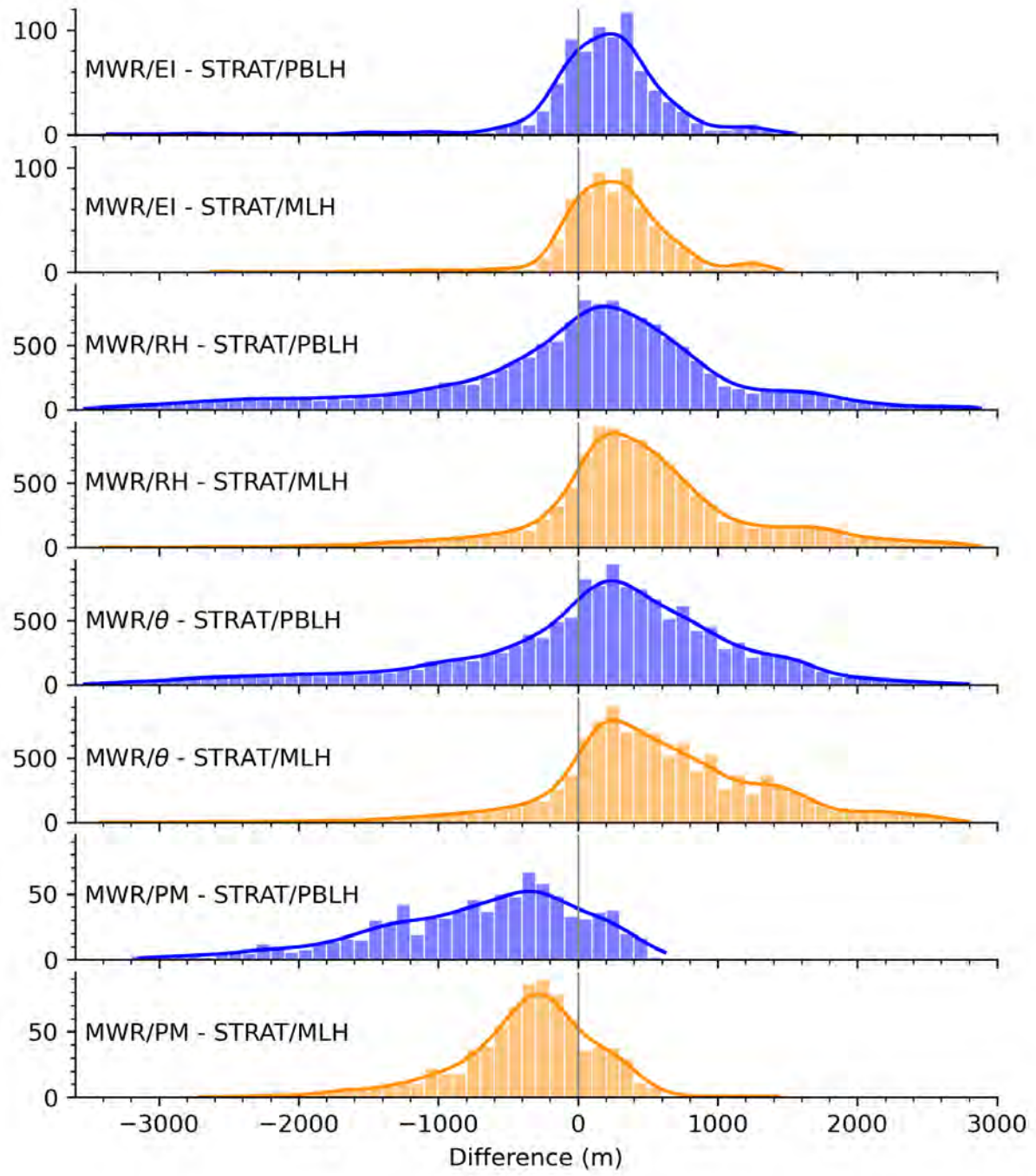

Figure 19: Comparison of STRAT/PBLH (blue) and STRAT/MLH (orange) to thermodynamic methods applied to the MWR. The y axis in each case is the count of observations in each 100 m interval. Note that the y axis has a different scale for the PM and EI methods due to the smaller number of time points at which the conditions for this method were met. The line indicates an approximate density function based on a Gaussian kernel density estimation function. The vertical grey line simply highlights 0 m and is not a property of the distributions.

		Without Processing					Removing Clouds				
Method		All	MO	DT	EV	NT	All	MO	DT	EV	NT
	N_t	13999	2276	2944	2265	6514	6236	1007	1537	1053	2639
EI	N	824	143	108	98	475	191	37	26	26	102
	P_{250} (%)	46.7	55.9	48.1	44.9	44.0	74.9	73.0	84.6	76.9	72.5
	a	0.12	-0.00	0.01	0.29	0.14	0.08	-0.32	-0.04	0.12	0.14
	b (m)	1341	1499	1493	1171	1300	1411	2025	1530	1541	1282
	R^2	0.02	0.00	0.00	0.15	0.03	0.01	0.17	0.01	0.02	0.03
	R^2_{one}	-1.75	-1.62	-2.60	-1.17	-1.75	-1.45	-2.66	-4.36	-1.24	-1.08
	M_Δ (m)	208	80	190	303	221	-2	-39	24	43	-13
	MAE (m)	357	330	399	352	357	301	318	286	351	287
RH	N	13778	2243	2909	2226	6400	6225	1005	1535	1051	2634
	P_{250} (%)	25.9	24.9	25.3	27.4	26.1	35.4	36.8	34.5	35.7	35.1
	a	0.07	0.01	0.09	0.13	0.05	0.11	0.07	0.14	0.12	0.09
	b (m)	1867	1899	1903	1809	1868	1639	1604	1680	1703	1607
	R^2	0.01	0.00	0.02	0.03	0.01	0.03	0.02	0.05	0.04	0.03
	R^2_{one}	-1.85	-2.27	-1.69	-1.40	-2.02	-2.78	-4.03	-2.06	-2.05	-3.58
	M_Δ (m)	139	147	139	145	126	-93	-128	-20	-35	-156
	MAE (m)	767	799	744	725	781	687	719	654	658	706
Θ	N	13806	2249	2911	2229	6417	6222	1005	1533	1049	2635
	P_{250} (%)	24.0	23.9	21.4	22.6	25.6	29.0	30.4	26.3	23.2	32.4
	a	0.15	0.11	0.14	0.18	0.14	0.15	0.14	0.14	0.13	0.15
	b (m)	1813	1814	1886	1837	1782	1839	1764	1902	2035	1765
	R^2	0.04	0.02	0.04	0.06	0.04	0.04	0.03	0.03	0.03	0.04
	R^2_{one}	-1.32	-1.52	-1.27	-1.11	-1.42	-1.24	-1.38	-1.20	-1.21	-1.33
	M_Δ (m)	235	235	244	292	208	115	59	144	241	61
	MAE (m)	772	794	768	769	768	746	765	729	777	735
PM	N	876	52	699	51	74	527	15	482	24	6
	P_{250} (%)	22.4	32.7	19.2	33.3	37.8	15.4	6.7	14.9	25.0	33.3
	a	0.17	-0.04	0.18	0.05	0.10	0.19	0.01	0.21	0.05	0.14
	b (m)	1132	1424	1117	1282	1166	1082	1260	1053	1295	1065
	R^2	0.24	0.04	0.22	0.09	0.24	0.24	0.04	0.26	0.08	0.08
	R^2_{one}	-12.05	-30.53	-12.09	-36.96	-21.5	-12.04	-475.40	-11.38	-42.6	-9.57
	M_Δ (m)	-582	67	-715	-196	13	-723	-579	-734	-493	-341
	MAE (m)	791	547	857	682	405	1127	1075	896	927	401

Table 10: Statistical results for thermodynamic PBLH methods implemented on MWR profiles (y) and STRAT/PBLH (x) for the times of day defined in table 4. N_t gives the total number of time points in each period at which the PBLH methods were evaluated on MWR profiles.

Method		Without Processing					Removing Clouds				
		All	MO	DT	EV	NT	All	MO	DT	EV	NT
	N_t	13999	2276	2944	2265	6514	6236	1007	1537	1053	2639
EI	N	708	132	104	89	383	169	37	26	26	80
	P_{250} (%)	45.2	47.0	46.2	44.9	44.4	74.0	62.2	80.8	73.1	77.5
	a	0.15	-0.15	0.14	0.35	0.12	0.13	-0.79	-0.03	0.35	0.05
	b (m)	1320	1674	1325	1114	1351	1350	2640	1519	1177	1414
	R^2	0.02	0.015	0.02	0.14	0.01	0.02	0.31	0.00	0.11	0.00
	R^2_{one}	-1.43	-1.59	-1.07	-0.84	-1.82	-0.77	-1.52	-1.25	-0.31	-1.04
	M_Δ (m)	257	194	184	297	262	55	-1	15	104	76
	MAE (m)	353	336	349	367	356	270	305	226	322	251
RH	N	11010	1691	2789	2004	4526	4853	704	1448	904	1797
	P_{250} (%)	27.7	27.2	29.2	26.9	27.3	40.3	42.9	40.0	36.6	41.3
	a	0.20	0.11	0.21	0.16	0.19	0.25	0.16	0.29	0.13	0.16
	b (m)	1696	1739	1715	1786	1706	1457	1502	1453	1683	1537
	R^2	0.03	0.00	0.04	0.02	0.02	0.07	0.01	0.10	0.02	0.02
	R^2_{one}	-1.00	-1.08	-0.84	-0.98	-1.14	-0.75	-0.77	-0.55	-1.07	-0.98
	M_Δ (m)	402	408	300	365	468	228	257	148	150	265
	MAE (m)	664	638	626	693	684	480	436	482	563	455
Θ	N	11035	1698	2791	2008	4538	4851	704	1446	903	1798
	P_{250} (%)	24.3	26.3	25.3	20.5	24.6	29.5	0.06	30.4	19.2	31.8
	a	0.27	0.13	0.26	0.19	0.33	0.25	0.06	0.26	0.10	0.26
	b (m)	1684	1787	1719	1863	1589	1734	1871	1728	2104	1684
	R^2	0.05	0.01	0.06	0.03	0.04	0.04	0.00	0.06	0.01	0.02
	R^2_{one}	-1.02	-1.15	-0.81	-1.08	-1.17	-0.89	-0.99	-0.66	-1.14	-1.05
	M_Δ (m)	489	491	386	472	576	388	370	299	442	472
	MAE (m)	731	714	682	778	747	696	657	630	805	708
PM	N	808	45	659	49	55	491	11	454	22	4
	P_{250} (%)	34.5	51.1	31.1	36.7	60	27.3	72.7	26.0	31.8	25.0
	a	0.25	-0.13	0.27	-0.02	0.08	0.29	-0.14	0.30	-0.09	-0.34
	b (m)	1038	1554	1013	1420	1211	971	1494	955	1564	1894
	R^2	0.28	0.04	0.27	0.00	0.05	0.28	0.23	0.29	0.05	0.20
	R^2_{one}	-3.79	-3.53	-4.00	-8.55	-7.17	-3.81	-27.90	-3.84	-9.22	-7.67
	M_Δ (m)	-309	119	-367	83	165	-413	-127	-420	-158	-376
	MAE (m)	474	266	513	402	246	546	232	556	514	426

Table 11: Statistical results for thermodynamic PBLH methods implemented on MWR profiles (y) and STRAT/MLH (x) for the times of day defined in table 4. N_t gives the total number of time points in each period at which the PBLH methods were evaluated on MWR profiles.

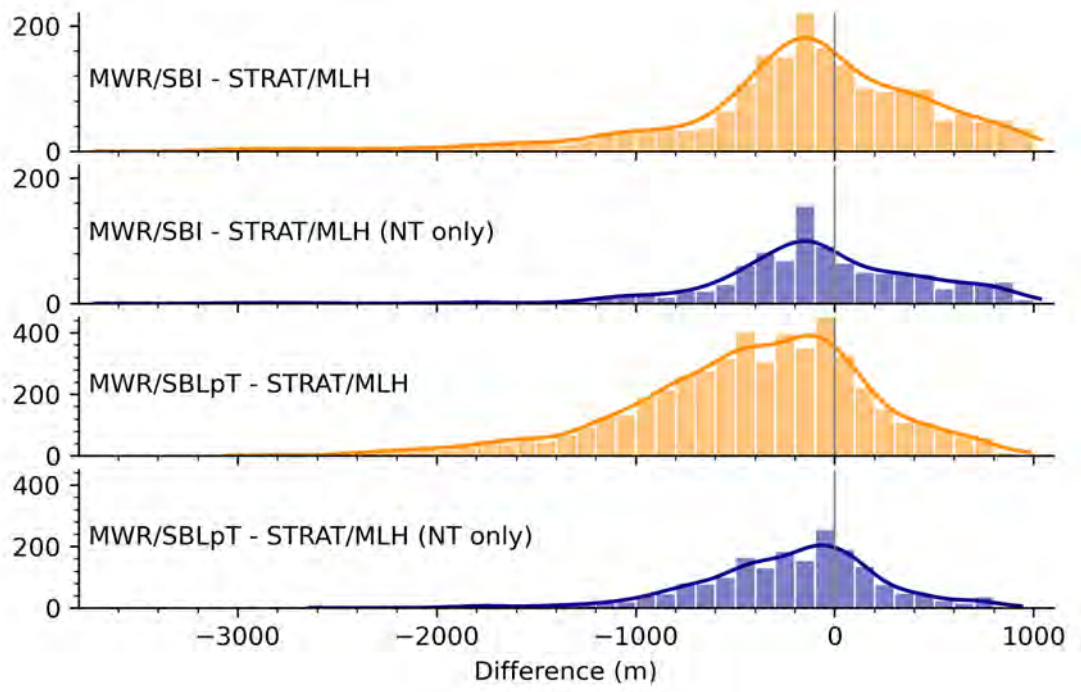

Figure 20: Comparison of STRAT/MLH to the nocturnal SBL methods methods applied to the MWR, at all times (orange) and at night only (dark blue). The y axis in each case is the count of observations in each 100 m interval. The line indicates an approximate density function based on a Gaussian kernel density estimation function. The vertical grey line simply highlights 0 m and is not a property of the distributions.

		Without Processing		**Removing Clouds**	
Method		All	NT	All	NT
	N_t	13999	6514	6236	2639
SBI	N	2063	1007	1044	512
	P_{100} (%)	14.8	15.6	15.4	15.4
	a	-0.11	-0.12	-0.07	-0.12
	b (m)	1390	1391	1264	1302
	R^2	0.04	0.02	0.03	0.04
	R^2_{one}	-4.24	-2.08	-9.37	-4.38
	M_Δ (m)	-129	-109	-177	-168
	MAE (m)	488	406	476	376
SBLpT	N	5155	1950	2448	779
	P_{100} (%)	15.4	23.1	9.8	16.3
	a	0.04	0.06	-0.01	-0.06
	b (m)	1182	1150	1296	1361
	R^2	0.01	0.01	0.00	0.01
	R^2_{one}	-8.14	-3.34	-10.00	-3.74
	M_Δ (m)	-356	-172	-488	-264
	MAE (m)	556	380	646	419

Table 12: Statistical results for thermodynamic, nocturnal SBL methods implemented on MWR profiles (y) and STRAT/MLH(x). N_t gives the total number of time points in each period at which the PBLH methods were evaluated on MWR profiles.

6 Conclusion

To assess method and instrument performance under varying atmospheric conditions, PBLH detection methods were implemented and compared at the CLOUDLAB field site, which is situated in hilly terrain. Thermodynamic PBLH estimation methods (EI, Θ, RH, PM, SBI, SBLpT) were implemented on profiles measured by RS, UAVs and an MWR. Aerosol backscatter methods were also investigated, by evaluating the proprietary algorithm of the ALC and by implementing the research algorithm STRATfinder to run on data from the ALC. The conclusions are divided according to the three aims introduced in section 1.1:

1. **Method Comparisons**

   For PBLH detection by the ALC, the manufacturer algorithm showed better agreement with STRAT/MLH ($P_{250} = 67.2\%$) than with STRAT/PBLH ($P_{250} = 46.4\%$), suggesting that the manufacturer algorithm detects the SBL rather than the RL at night. This was supported by case study observations for days with a clear diurnal evolution. On a systematic level for one year of observations, the PBLH estimated by thermodynamic methods applied to MWR profiles demonstrated poor agreement to STRAT/PBLH and STRAT/MLH. Each thermodynamic method has characteristics which should be considered before operational implementation. The RH and Θ methods rely on peak detection, and the detected peak may not be a concrete signature of the PBLH. In contrast, an elevated temperature inversion, if present, appears to be a more robust signature of the PBLH which agrees well with the aerosol distribution as determined by STRAT/PBLH. The PM yielded an underestimation of the PBLH compared to STRAT/MLH and STRAT/PBLH. The criteria for thermodynamic SBL detection were not met consistently during the night, and were often also met during the day. The agreement of the SBL top detected by thermodynamic methods to STRAT/MLH was low.

2. **Instrument Comparisons**

   When the PBLH signature is strong (such as an elevated temperature inversion) and the UAV profile goes high enough, the PBLH estimated by the same method applied to RS and UAV profiles shows high agreement. For the less strict Θ and RH methods, the agreement is poorer. The smoothness of the MWR profiles means that inversions are often not detected. For methods which rely on peak detection, the low-resolution MWR profiles have fewer local peaks than the RS and UAV profiles, leading to differences in the detected PBLH. For all instrument comparisons, the agreement is especially poor for the SBLpT method, which can be attributed to differences in the temperature profiles close to the ground.

3. **Atmospheric Conditions**

   Analysis of the backscatter evolution and the detected PBLH revealed that the ideal diurnal evolution with a distinct CBL, RL and nocturnal SBL occurred rarely at the field site (fewer than five days in the dataset of 372 days). When the ideal evolution did occur, the maximum CBL height occurred later in the day (late afternoon) than reported by previous studies for other locations. However, the small number of clear days meant that this could not be conclusively assessed. Method comparisons split by the time of day relative to sunrise did not reveal strong differences in agreement. This can be partly explained by the lack of a clear diurnal evolution on most days. Case study analysis revealed that the presence of clouds leads to large differences in the PBLH detected by the thermodynamic and aerosol methods. However, for comparisons over the whole year, removing all time points with low clouds did not result in a systematic improvement in method agreement.

Concluding comments can also be made on the three novel aspects of this study compared to previous PBLH studies:

1. **UAV Measurements**

   This study showed that raw profiles from UAVs are capable of capturing the same thermodynamic PBLH signatures as RS profiles. A clear advantage of UAVs compared to RS is their ability to fly vertically to measure a profile above a desired location. To avoid the issue of false layer detection due to short profiles, it is recommended that UAV flights for PBLH detection fly to at least 3000 m AGL. The UAV raw profiles have a high vertical resolution compared to RS and the MWR, but this means that some smoothing is required before PBLH detection methods are applied. The high resolution could be advantageous for SBL detection due to the smaller distances involved. However, the agreement of the UAV profiles to the RS and MWR profiles was lowest close to the ground, leading to low confidence in the resulting SBI and SBLpT detections. If UAVs were launched automatically on a regular basis, the profiles would provide more information on the thermodynamic PBL structure than the low resolution MWR profiles. However, a widespread replacement of operational RS profiles by regular UAV flights would require high flight consistency and transparent, validated data processing routines.

2. **Hilly Terrain**

   Since no comparisons were made to a site with flatter or more complex terrain, the direct influence of the hilly terrain on the PBLH development or method agreement cannot be assessed. However, method agreement over the year was generally poorer than that reporded by previous studies and this can be tentatively attributed to the hilly terrain. For example, the elevated position leads to the regular occurrence of fog in the winter, which causes high backscatter close to the ground and the failure of the aerosol PBLH methods. In addition, the hilly terrain is expected to reduce the accuracy of the MWR profiles themselves, since the specific topography is not well-represented in the 30 km grid of the ERA reanalysis dataset, on which the retrievals are based. Dynamical influences of the terrain on the turbulent flow in the PBL are not captured by thermodynamic profiles above the single field site. Investigating method comparisons under different wind directions could help assess the influence of different terrain elements around the site on the PBL structure.

3. **Winter Data Availability**

   The fact that UAV and RS profiles were only available during winter and spring meant that the PBLH estimations of the MWR could not be evaluated by in situ measurements during the summer and autumn, and could instead only be compared with the aerosol methods. In addition, the stability close to the ground meant that PM or Richardson method could not be used on the RS or UAV profiles. The sensitivity of the PM to the high smoothness of the MWR profiles could therefore not be assessed.

At Eriswil, the infrequent occurrence of days in which the PBL shows an ideal diurnal evolution means that standard PBLH detection methods do not show high agreement with each other. Indeed, on many days the prevalence of low-level clouds means that the PBLH would be difficult to determine from the backscatter evolution even by an experienced specialist. Without a robust conditions classification and quality checking system, fully automated PBLH detection at the CLOUDLAB field site is not feasible.

Acknowledgements

A huge thank you to Robert for the relaxed and kind supervision of this project. Thanks to Gunter for the official supervision in Bern and for the warm welcome into the microwave physics group. I would like to thank Martine Collaud Coen and Alexandre Bugnard for the interesting presentation exchanges and Maxime Hervo for generating the overlap model for the Eriswil ceilometer. Thanks to the whole CLOUDLAB team for the chance to help out in the field campaign: it was great fun, even at 4am after 5 hours in the cold! Finally, thank you to the other master students of the Oeschger Centre for all the sunny lunchtimes.

References

J. N. Aryee, L. K. Amekudzi, K. Preko, W. A. Atiah, and S. K. Danuor. Estimation of planetary boundary layer height from radiosonde profiles over West Africa during the AMMA field campaign: Intercomparison of different methods. *Scientific African*, 7:e00228, 2020. doi:10.1016/J.SCIAF.2019.E00228.

N. Babić, B. Adler, A. Gohm, N. Kalthoff, M. Haid, M. Lehner, P. Ladstätter, and M. W. Rotach. Cross-valley vortices in the Inn valley, Austria: Structure, evolution and governing force imbalances. *Quarterly Journal of the Royal Meteorological Society*, 147(740):3835–3861, 2021. doi:10.1002/qj.4159.

L. Bianco, K. Friedrich, J. M. Wilczak, D. Hazen, D. Wolfe, R. Delgado, S. P. Oncley, and J. K. Lundquist. Assessing the accuracy of microwave radiometers and radio acoustic sounding systems for wind energy applications. *Atmospheric Measurement Techniques*, 10(5):1707–1721, 2017. doi:10.5194/amt-10-1707-2017.

D. Bolton. The computation of equivalent potential temperature. *Monthly Weather Review*, 108(7): 1046–1053, 1980. doi:10.1175/1520-0493(1980)108<1046:TCOEPT>2.0.CO;2.

A. Bugnard. Comparison between ground-based remote sensing observations and NWP model profiles in a complex topography: The Meiringen campaign. Master's thesis, École Polytechnique Fédérale de Lausanne, 2023. Shortly to be published at https://infoscience.epfl.ch.

M. P. Cadeddu, V. P. Ghate, D. D. Turner, and T. E. Surleta. Boundary layer moisture variability at the Atmospheric Radiation Measurement (ARM) Eastern North Atlantic observatory during marine conditions. *Atmospheric Chemistry and Physics*, 23(6):3453–3470, 2023. doi:10.5194/acp-23-3453-2023.

D. Cimini, M. Haeffelin, S. Kotthaus, U. Löhnert, P. Martinet, E. O'Connor, C. Walden, M. Collaud Coen, and J. Preissler. Towards the profiling of the atmospheric boundary layer at European scale—introducing the COST Action PROBE. *Bulletin of Atmospheric Science and Technology*, 1(1): 23–42, 2020. doi:10.1007/s42865-020-00003-8.

M. Collaud Coen, C. Praz, A. Haefele, D. Ruffieux, P. Kaufmann, and B. Calpini. Determination and climatology of the planetary boundary layer height above the Swiss plateau by in situ and remote sensing measurements as well as by the COSMO-2 model. *Atmospheric Chemistry and Physics*, 14(23): 13205–13221, 2014. doi:10.5194/ACP-14-13205-2014.

J. Cuxart. Atmospheric boundary-layer over complex terrain. Report from ECMWF GABLS workshop on diurnal cycles and the stable boundary layer, 7-10 November. Available at `https://www.ecmwf.int/sites/default/files/elibrary/2012/7462-contents.pdf` (Accessed: 2023-3-28), 2011.

R. Dang, Y. Yang, X. M. Hu, Z. Wang, and S. Zhang. A review of techniques for diagnosing the atmospheric boundary layer height (ABLH) using aerosol lidar data. *Remote Sensing*, 11(13), 2019. doi:10.3390/RS11131590.

S. Emeis, K. Schäfer, and C. Münkel. Surface-based remote sensing of the mixing-layer height - a review. *Meteorologische Zeitschrift*, 17(5):621–630, 2008. doi:10.1127/0941-2948/2008/0312.

S. Finardi, J. Erbrink, B. Fisher, and European Commission and Directorate-General for Research and Innovation. COST Action 710 - final report: Harmonisation of the pre-processing of meteorological data for atmospheric dispersion models. Available at `https://op.europa.eu/en/publication-detail/-/publication/e2f3628d-3e05-4477-96c3-81c868a3d2e6/language-en` (Accessed: 2023-3-28), 1998.

T. Foken, editor. *Springer Handbook of Atmospheric Measurements*. Springer Nature Switzerland AG, 2022. doi:https://doi.org/10.1007/978-3-030-52171-4.

M. Hervo, Y. Poltera, and A. Haefele. An empirical method to correct for temperature-dependent variations in the overlap function of CHM15k ceilometers. *Atmospheric Measurement Techniques*, 9(7): 2947–2959, 2016. doi:10.5194/AMT-9-2947-2016.

B. Heutte. Climatology of atmospheric boundary layer height over Switzerland. Master's thesis, École Polytechnique Fédérale de Lausanne, 2021. Available at `https://infoscience.epfl.ch/record/295181` (Accessed: 2023-3-24).

C. Ketterer, P. Zieger, N. Bukowiecki, M. Collaud Coen, O. Maier, D. Ruffieux, and E. Weingartner. Investigation of the planetary boundary layer in the Swiss Alps using remote sensing and in situ measurements. *Boundary-Layer Meteorology*, 151(2):317–334, 2014. doi:10.1007/s10546-013-9897-8.

S. Kotthaus and C. S. B. Grimmond. Atmospheric boundary-layer characteristics from ceilometer measurements. part 1: A new method to track mixed layer height and classify clouds. *Quarterly Journal of the Royal Meteorological Society*, 144(714):1525–1538, 2018. doi:10.1002/qj.3299.

S. Kotthaus, M. Haeffelin, M. A. Drouin, J. C. Dupont, S. Grimmond, A. Haefele, M. Hervo, Y. Poltera, and M. Wiegner. Tailored algorithms for the detection of the atmospheric boundary layer height from common automatic lidars and ceilometers (ALC). *Remote Sensing*, 12(19):1–23, 2020. doi:10.3390/rs12193259.

S. Kotthaus, J. A. Bravo-Aranda, M. Collaud Coen, J. L. Guerrero-Rascado, M. J. Costa, D. Cimini, E. J. O'Connor, M. Hervo, L. Alados-Arboledas, M. Jiménez-Portaz, L. Mona, D. Ruffieux, A. Illingworth, and M. Haeffelin. Atmospheric boundary layer height from ground-based remote sensing: A review of capabilities and limitations. *Atmospheric Measurement Techniques*, 16(2):433–479, 2023. doi:10.5194/amt-16-433-2023.

R. Krishnamurthy, R. K. Newsom, L. K. Berg, H. Xiao, P. L. Ma, and D. D. Turner. On the estimation of boundary layer heights: A machine learning approach. *Atmospheric Measurement Techniques*, 14(6): 4403–4424, 2021. doi:10.5194/AMT-14-4403-2021.

M. Lehner and M. W. Rotach. Current challenges in understanding and predicting transport and exchange in the atmosphere over mountainous terrain. *Atmosphere*, 9(7):276, 2018. doi:10.3390/atmos9070276.

H. Li, B. Liu, X. Ma, S. Jin, Y. Ma, Y. Zhao, and W. Gong. Evaluation of retrieval methods for planetary boundary layer height based on radiosonde data. *Atmospheric Measurement Techniques*, 14 (9):5977–5986, 2021. doi:10.5194/AMT-14-5977-2021.

Lufft. Manual Ceilometer CHM 15k NIMBUS . G. Lufft Mess- und Regeltechnik GmbH. Instrument Manual available at `https://s.campbellsci.com/documents/ca/manuals/chm15k_man.pdf` (Accessed: 2023-3-28), 2016.

G. Martucci, R. Matthey, V. Mitev, and H. Richner. Comparison between backscatter lidar and radiosonde measurements of the diurnal and nocturnal stratification in the lower troposphere. *Journal of Atmospheric and Oceanic Technology*, 24(7):1231 – 1244, 2007. doi:10.1175/JTECH2036.1.

Y. Morille, M. Haeffelin, P. Drobinski, and J. Pelon. STRAT: An automated algorithm to retrieve the vertical structure of the atmosphere from single-channel lidar data. *Journal of Atmospheric and Oceanic Technology*, 24(5):761–775, 2007. doi:10.1175/JTECH2008.1.

Y. Pan, Z. Jin, P. Tong, W. Xu, and W. Wang. Edge detection method for determining boundary layer height based on Doppler lidar. *Atmosphere*, 12(9), 2021. doi:10.3390/atmos12091103.

J. Portmann. Drones: Can they accurately measure the atmosphere? Unpublished bachelor thesis, ETH Zürich., 2022.

Radiometer Physics GmbH. RPG-HATPRO measurements. Report available at `https://www.radiometer-physics.de/download/Radiometer/HATPRO/Info/HATPRO%20Measurement%20Examples.pdf` (Accessed: 2023-3-28), 2008.

Radiometer Physics GmbH. Operation principles and software description for RPG standard single polarization radiometers (G5 series). Instrument Operation and Software Guide available at `https://www.radiometer-physics.de/download/PDF/Radiometers/HATPRO/RPG_MWR_STD_Software_Manual%20G5.pdf` (Accessed: 2023-3-28), 2014.

T. Rieutord, S. Aubert, and T. Machado. Deriving boundary layer height from aerosol lidar using machine learning: KABL and ADABL algorithms. *Atmospheric Measurement Techniques*, 14(6):4335–4353, 2021. doi:10.5194/amt-14-4335-2021.

M. W. Rotach and D. Zardi. On the boundary-layer structure over highly complex terrain: Key findings from MAP. *Quarterly Journal of the Royal Meteorological Society*, 133(625 B):937–948, 2007. doi:10.1002/qj.71.

P. Seibert, F. Beyrich, S. E. Gryning, S. Joffre, A. Rasmussen, and P. Tercier. Review and intercomparison of operational methods for the determination of the mixing height. *Atmospheric Environment*, 34(7): 1001–1027, 2000. doi:10.1016/S1352-2310(99)00349-0.

D. J. Seidel, C. O. Ao, and K. Li. Estimating climatological planetary boundary layer heights from radiosonde observations: Comparison of methods and uncertainty analysis. *Journal of Geophysical Research: Atmospheres*, 115(D16):16113, 2010. doi:10.1029/2009JD013680.

D. J. Seidel, Y. Zhang, A. Beljaars, J.-C. Golaz, A. R. Jacobson, and B. Medeiros. Climatology of the planetary boundary layer over the continental United States and Europe. *Journal of Geophysical Research: Atmospheres*, 117(D17):17106, 2012. doi:10.1029/2012JD018143.

R. Stull. *An Introduction to Boundary Layer Meteorology*. Kluwer Academic Publishers, 1988. doi:10.1007/978-94-009-3027-8.

D. D. Turner and U. Lohnert. Ground-based temperature and humidity profiling: Combining active and passive remote sensors. *Atmospheric Measurement Techniques*, 14(4):3033–3048, 2021. doi:10.5194/amt-14-3033-2021.

X. Y. Wang and K. C. Wang. Estimation of atmospheric mixing layer height from radiosonde data. *Atmospheric Measurement Techniques*, 7(6):1701–1709, 2014. doi:10.5194/amt-7-1701-2014.

S. S. Zilitinkevich, S. A. Tyuryakov, Y. I. Troitskaya, and E. A. Mareev. Theoretical models of the height of the atmospheric boundary layer and turbulent entrainment at its upper boundary. *Izvestiya - Atmospheric and Ocean Physics*, 48(1):133–142, 2012. doi:10.1134/S0001433812010148.

Appendices

A Data

A.1 Unmanned Aerial Vehicle Data

Figure 21 gives an example of UAV data, for three variables relevant for the thermodynamic methods (section 4.2) The raw data is recorded at a frequency of 20 Hz, so has a vertical resolution which depends on the ascent speed. The raw data was smoothed to 5 m and 10 m intervals using the mean and median. The difference between these smoothed profiles and the raw profile is very small. However, regular height intervals are helpful for the application of the Savitzky–Golay method for gradient calculations (appendix B.4). I therefore decided to use the 5 m median profiles. The processed data supplied by the UAV manufacturer shows noticeable differences to the raw data for all UAV profiles. However, the direction or size of the offset for the temperature and *RH* is not consistent. In the example in figure 21, the *RH* profile processed data shows smaller variation near the top of the profile, which would have an influence on gradient peaks detected in the RH method (section 2.2.2). The variation in pressure between the raw and processed data is very small for all profiles. The processed data was evaluated against RS profiles by Portmann (2022). The agreement for temperature profiles was found to be higher than for *RH* profiles. Since the manufacturer processing steps are unknown, I decided to use the raw data in my project. A systematic comparison of the raw and processed profiles or the resulting PBLH estimations was not completed.

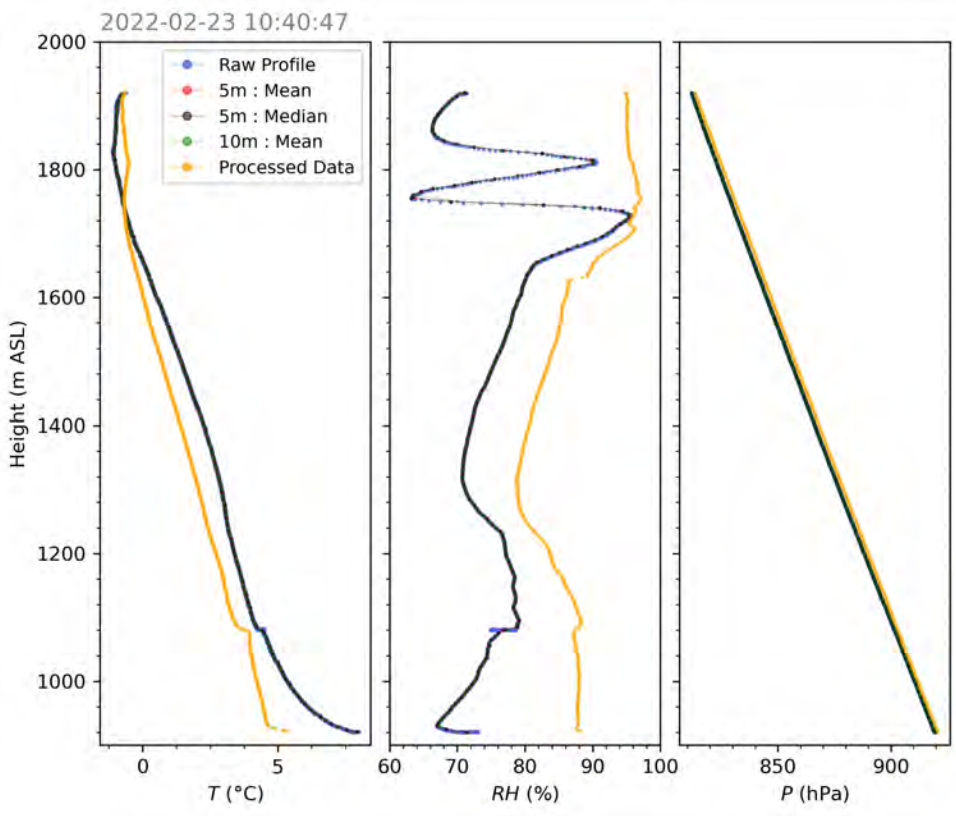

Figure 21: An example of UAV raw and processed data. The raw data averaged to 5 m intervals using the median was used for all further analysis in this project.

A.2 Microwave Radiometer Resolution

Figure 22 gives the vertical resolution of the MWR temperature and humidity profiles used in this project. The varying resolution arises from the weighting functions applied to the different frequency channels (Radiometer Physics GmbH, 2014).

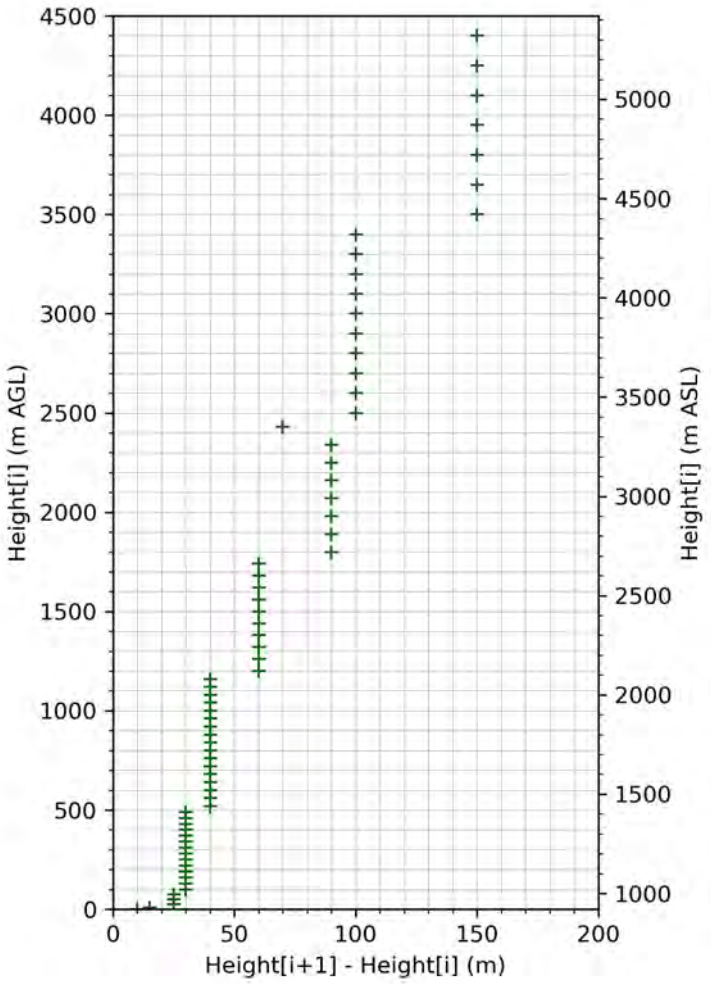

Figure 22: The vertical resolution of the temperature and humidity profiles from the MWR. The x axis gives the difference between the successive height points. Note that the jump at 1200 m AGL indicates the transition from the boundary layer scans to the zenith profile. The field site is at 920 m ASL.

B Methods

B.1 Hydro-static Pressure Calculation

Calculation of the potential temperature θ requires knowledge of the pressure p. In the absence of in-situ pressure measurements, the potential temperature can still be calculated if the the PBL is assumed to be in vertical hydro-static equilibrium (Collaud Coen et al., 2014):

$$\frac{\partial p}{\partial z} = -\rho g, \tag{2}$$

where z is the geometrical height coordinate, g is the gravitational acceleration (approximated as constant at 9.81 ms^{-2} throughout the boundary layer) and ρ is the density of air, which depends on the temperature according to the ideal gas law (neglecting the effect of moisture).

$$p = \rho R_d T, \tag{3}$$

where R_d is the gas constant for dry air (287.053 $\mathrm{JK}^{-1}\mathrm{kg}^{-1}$). The pressure is then found from the temperature profile $T(z)$ according to

$$p(z, T) = p_0 \cdot \exp\left(-\int_{z_0}^{z} \frac{g}{R_d T\left(z'\right)} \mathrm{d}z'\right), \tag{4}$$

where p_0 is the pressure at height z_0. In practice, I integrated step-wise from the surface pressure measured by the MWR surface weather station:

$$p(z_i) = p(z_{i-1}) * (1 - \frac{g}{R_d T(z_{i-1})}) * (z_i - z_{i-1}). \tag{5}$$

B.2 Relative Humidity Calculation

For the MWR profiles, I calculated the relative humidity RH from the absolute humidity ρ_v. The water vapour pressure e is first calculated according to the ideal gas law:

$$e = \rho_v R_v T, \tag{6}$$

where T is the temperature in Kelvin and R_v is the gas constant for water vapour (461.52 $\mathrm{JK}^{-1}\mathrm{kg}^{-1}$). The saturation vapour pressure e_s is calculated according to the formula presented by Bolton (1980). This is the same formula as used in the Python library MetPy.

$$e_s = e_0 \exp\left(\frac{17.67(T - 273.15)}{T - 29.65}\right), \tag{7}$$

where e_0 is the triple point vapour pressure of water (611.2 Pa). Finally, RH is calculated in percent as

$$RH = \frac{e}{e_s} * 100\%. \tag{8}$$

B.3 Richardson Method

The flux Richardson number Ri_f describes the ratio of buoyant consumption and shear production of turbulent kinetic energy (Stull, 1988):

$$Ri_f = \frac{\left(\frac{g}{\overline{\theta}}\right)\left(\overline{w'\theta'}\right)}{\left(\overline{u'w'}\right)\frac{\partial\overline{u}}{\partial z} + \left(\overline{v'w'}\right)\frac{\partial\overline{v}}{\partial z}}, \tag{9}$$

where $\overline{w'\theta'}$ is proportional to the vertical turbulent flux of sensible heat, $\overline{u'w'}$ and $\overline{v'w'}$ are proportional to the vertical fluxes of horizontal momentum and $\frac{\partial\overline{u}}{\partial z}$ and $\frac{\partial\overline{v}}{\partial z}$ are the vertical gradients of the mean horizontal velocities. In the absence of flux measurements, the fluxes can be parameterised as proportional to the mean vertical gradients (Stull, 1988). If the gradients are additionally approximated using discrete differences, the bulk Richardson number Ri_b can be calculated from profile measurements:

$$Ri_b = \frac{g\Delta z\Delta\theta}{\overline{\theta}\left((\Delta\overline{u})^2 + (\Delta\overline{v})^2\right)}, \tag{10}$$

where Δ indicates a difference between the value at height z and the value at the surface. There is some variation in the value $\overline{\theta}$ taken for normalisation. Collaud Coen et al. (2014) use the mean θ between the surface and height z, to be consistent with the Ri_b implementation in the COSMO model. The COSMO formulation also assumes that the horizontal winds $\overline{u}$ and $\overline{v}$ are zero at the surface. Other authors normalise by θ_0 (Seidel et al., 2012) or by θ measured at the height z (Seibert et al., 2000).

The PBLH is taken as the first height z at which Ri_b is greater than a threshold value, often 0.25 (Kotthaus et al., 2023; Li et al., 2021; Seibert et al., 2000; Seidel et al., 2012). This corresponds to the height at which buoyant damping of turbulence outweighs shear production, marking the top of the turbulent PBL. Collaud Coen et al. (2014) use threshold values of 0.22 during the day and 0.33 in the night. However, due to the small change of Ri_b with height in this region, the impact of the exact threshold on the PBLH is small (Collaud Coen et al., 2014; Seidel et al., 2012).

The PM and Richardson number method are identical if the threshold value is set to zero, so the Richardson number method will always give a greater PBLH than the PM (by around 20 m for the CBL - Collaud Coen et al., 2014). Since it accounts for the influence of wind shear on vertical mixing, the Richardson method should be preferred over the PM in cases where the wind shear is relevant (Seibert et al., 2000). The Richardson method was chosen by Seidel et al. (2012) for their climatology of PBLH, since it can be applied in stable and unstable conditions and is not strongly dependent on the vertical resolution of RS profiles. The Richardson number method is also used to determine the PBLH in the ERA-interim analysis (Kotthaus et al., 2023). The method may fail in very stable conditions, if the bulk Richardson number at the surface is already higher than the threshold value (Collaud Coen et al., 2014).

B.4 Gradient Calculation

Figure 23 shows the effect of using different window sizes in the Savitzky–Golay filter for the potential temperature gradient, and the effect of this on the PBLH detection by the Θ method (section 4.2.3) and SBL top detection by the SBLpT method (section 4.2.6). The Θ method detects the *biggest* peak in the potential temperture gradient, so the profile smoothness has a very low effect on the PBLH, since smoothing is unlikely to change which peak is the biggest. The same holds for the RH method, where the minimum peak in the vertical gradient is detected (not shown). In contrast, the SBLpT method detects the *lowest* peak below the threshold of 0.003 Km^{-1}. Smooth profiles have fewer local peaks, so the lowest peak is likely to be at a higher height. For example, the SBLpT detected in figure 23a is higher for a window length of 380 m than for a window length of 140 m. Overall, the sensitivity to the polynomial order (not shown) and window size was found to be rather low. Window sizes of 300 m and 305 m were chosen for the RS and UAV profiles respectively, to avoid having too many local peaks. Figure 23b also shows the ambiguity associated with UAV flights which reach low heights. Although a maximum peak is detected (dashed blue line), only with the RS and MWR profiles can it be seen that this peak is unlikely to be the PBLH. Finally, figure 23 shows the large profile disagreement close to the ground, including a local peak in the MWR profile which does not appear in the RS and UAV profiles. The lower limit for PBLH detection was therefore set to 1200 m for the EI, PM, RH, Θ methods and to 950 m for the SBI and SBLpT methods.

B.5 STRATfinder Configuration

Table 13 gives the configuration parameters used for the STRATfinder algorithm at Eriswil. The key difference compared to those used in the initial evaluation of STRATfinder (Kotthaus et al., 2020) is the 'calibration' parameter, which is 1.0 in this study. The ALC at the field site returns the attenuated backscatter, so the conversion from overlap and baseline corrected backscatter to attenuated backscatter does not have to take place within STRATfinder. The sensitivity of the detected MLH to the parameters 'growth_onset' and 'growth_rate' was briefly investigated. Based on a year of backscatter plots such as those in section 5.1 and approximate PBLH determination by eye, the time at which growth of the MLH commenced agreed well with the three hours after sunrise used within STRATfinder. Setting a smaller 'growth_onset' of two hours or one hour resulted in a detected MLH which appeared to grow faster than the strong change in backscatter, or showed jumps early in the morning (figures not shown). The 'growth_rate' parameter is higher than growth rates estimated from the backscatter plots (typically 100 mh^{-1} to 200 mh^{-1} on days showing ideal MLH evolution). However, setting this parameter too high is not expected to lead to large changes in the detected MLH, since it controls the search region for the MLH, rather than the MLH itself. For an example day, changing this parameter as high as 2000 mh^{-1} resulted in no change in the detected MLH. In contrast, if this parameter is too small, the search region may not extend high enough for the MLH to be detected by the pathfinder approach. On days when the detected MLH showed an especially high growth rate, the PBL often showed non-ideal diurnal evolution (for example, due to extensive cloud cover). In these cases, setting the 'growth_rate' parameter to a lower value is likely to have resulted in a *different* detected MLH, but not necessarily to higher agreement to other methods or a more physically meaningful detected layer. Extensive investigations into the sensitivity of PBLH detection to the other configuration thresholds were not undertaken in this study and apart from the 'calibration' parameter, the values chosen are the same as those used by Kotthaus et al. (2020) for the ALC at Payerne, Switzerland.

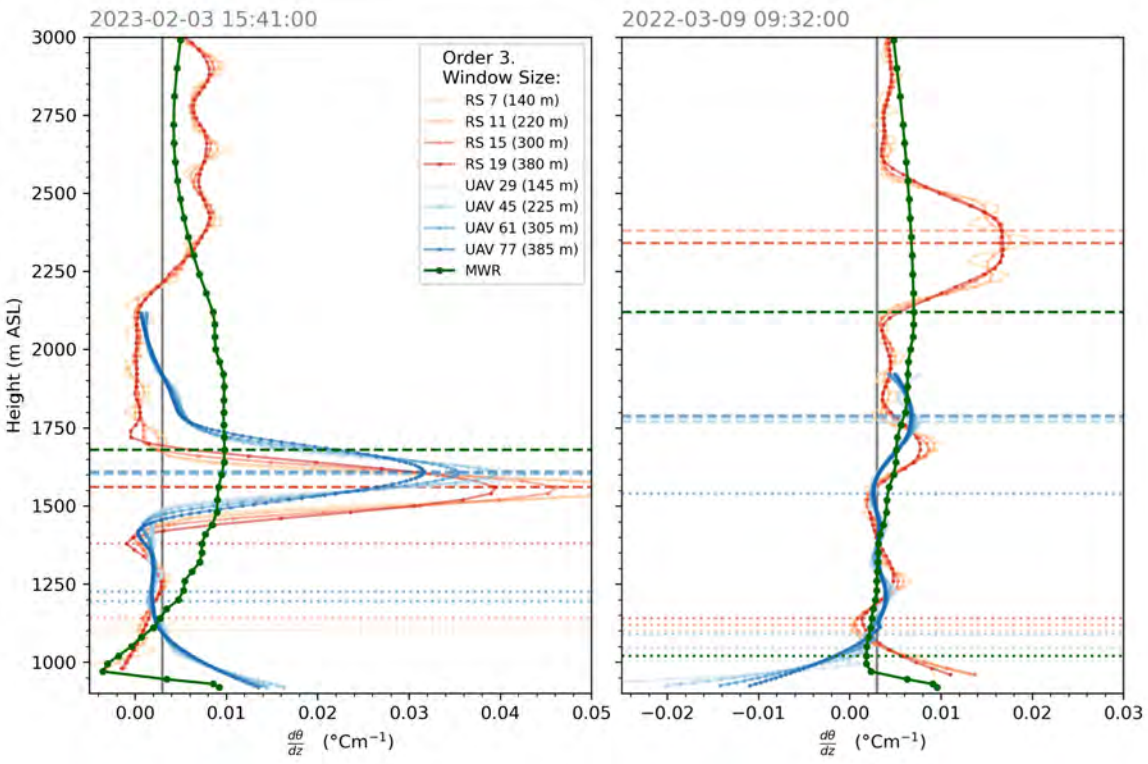

(a) (b)

Figure 23: Investigating gradient methods with the potential temperature gradient. For RS and UAV profiles, a Savitzky–Golay filter with polynomial order 3 and varying window size was used. The gradient from the MWR profile is shown for comparison and is calculated using second order finite differences. Dotted horizontal lines show the SBL top detected by the SBLpT method. Dashed horizontal lines show the PBLH detected by the Θ method. The grey vertical line shows the threshold of 0.003 Km^{-1} used for the SBLpT method. The legend gives the window size in points and metres, accounting for the vertical resolution of the RS data (20 m) and the resampled UAV data (5 m). The start times of each profile are the same as in figure 5 and figure 9.

Group	Parameter Name	Description	Value used in this study
Instrument	threshold_overlap	Profile only considered above this limit of optical overlap function	0.05
	calibration	Calibration factor for calculation of attenuated backscatter from overlap and baseline corrected backscatter	1.0
PBLH Setttings	threshold_molecular	Threshold used to identify lowest height in attenuated backscatter where particle scattering is negligible. Used to define the upper search region for PBLH.	10^{-7} $sr^{-1}m^{-1}$
	dayMax	Maximum of PBLH search region during day	4000 m AGL
	dayMin	Minimum of PBLH search region during day	0 m AGL
	evening	Maximum of PBLH search region during evening	2500 m AGL
	nightMax	Maximum of PBLH search region during night	700 m AGL
	nightMin	Minimum of PBLH search region during night	0 m AGL
MLH Settings	growth_onset	Delay of MLH growth onset relative to sunrise	3 h
	growth_rate	Growth rate of MLH from the growth onset, used to define the maximum height of the search region of MLH	300 mh^{-1}
Pathfinder	jump	Maximum allowed vertical displacement between two adjacent paths tracked by pathfinding algorithm	32.5 m
	pathfinder_window	Period considered for each implementation of pathfinding algorithm	1800 s
	threshold_gradient	Threshold to define regions of increased weights based on small or positive vertical gradients	-5×10^{-4} $sr^{-1}m^{-1}$
	threshold_log10variance	Threshold to define regions of increased weights based on low variance	10^{10}
Variance	highpassfilter	Timescale above which variance contributions are neglected (to remove mesoscale variability)	1800 s
	FFT_window	Time window for variance calculations	3600 s
	FFT_sample	Time resolution for variance calculations	600 s
	threshold_SNR	Signal to noise ratio threshold used for denoising the variance field	0.6745
Cloud Settings	threshold_cloud	Attenuated backscatter exceeding this value is excluded from variance calculations	$10^{-4.6}$ $sr^{-1}m^{-1}$
	cloud_window	Window size to smooth attenuated backscatter when creating cloud mask before variance calculations	11 time steps

Table 13: STRATfinder configuration parameters. The descriptions are adapted from Kotthaus et al. (2020) and the STRATfinder MATLAB code. Backscatter-related threshold are given in $sr^{-1}m^{-1}$ as in figure 12. However, the signal from the ALC may not be absolutely calibrated into attenuated backscatter and the same thresholds in Kotthaus et al. (2020) are given in arbitrary units a.u.

B.6 Statistical Metrics

For comparison between two vectors of PBLH observations $\mathbf{x}$ and $\mathbf{y}$ (with missing values already removed such that each element x_i has a corresponding element y_i and both vectors have length N), a number of statistical metrics are used (section 4.3).

The coefficient of determination R^2 is defined as

$$R^2 = 1 - \frac{SS_{regression}}{SS_{total}} \tag{11}$$

$$= 1 - \frac{\sum_{i=1}^{N}(y_i - \hat{y}_i)^2}{\sum_{i=1}^{N}(y_i - \overline{y})^2}, \tag{12}$$

where $SS_{regression}$ is the sum of squares of the residuals between the observations and the predicted values from a regression model, SS_{total} is the sum of squares between the elements y_i and the mean of all in elements in $\mathbf{y}$. For the coefficient of determination between the data and a linear model, $\hat{y}_i = ax_i + b$. For the coefficient of determination between the data and the $1:1$ line (R^2_{one}), $\hat{y}_i = x_i$. In each case, an R^2 close to 1 indicates that the variation in $\mathbf{y}$ is well accounted for by the model. With a constrained model such as the $1:1$ line, R^2 can be negative. This indicates that the variation in $\mathbf{y}$ is better explained by a horizontal line at $\overline{y}$ than by the regression model.

The median bias M_Δ is the median element of the difference $\mathbf{y} - \mathbf{x}$. The mean absolute error MAE is a measure of the absolute errors between the observations in $\mathbf{x}$ and $\mathbf{y}$:

$$MAE = \frac{1}{N}\sum_{i=1}^{N}|y_i - x_i|. \tag{13}$$

C Results

C.1 Instrument Comparison: Unmanned Aerial Vehicles and Microwave Radiometer

Figure 24 shows the comparison of the PBLH detected from the 69 UAV profiles and corresponding MWR profiles for the three methods EI, RH and Θ. The number of profiles in the times of day MO, DT, EV and NT was 23, 28, four and 14 respectively. No profiles took place during rain (using the rain flag of the surface weather station) but 39 profiles occurred at times with cloud bases lower than 5000 m ASL. As for the RS and MWR comparison (section 5.3.2), the EI method shows the best agreement between the two instruments. The agreement between the instruments increases when UAV profiles whose maximum height is below that of the PBLH detected by the MWR are removed. Figure 25 shows the comparison of the SBLpT method, split by the time of day relative to sunrise. No clear increase in agreement between the methods is observed during NT. Statistical metrics for the UAV and MWR instrument comparison are given in table 14.

	EI	**RH**	**Θ**	**SBLpT**
N	5	69 (52)	68 (26)	42
P_{250} (%)	100	42.6 (53.8)	30.9 (80.8)	16
a	0.33	-0.04 (-0.12)	-0.04 (0.29)	0.00
b (m)	1079	1582 (1710)	1620 (1101)	1139
R^2	0.26	0.01 (0.01)	0.01 (0.12)	0.00
R^2_{one}	-2.47	-7.23 (-1.63)	-9.98 (-0.71)	-2.50
M_Δ (m)	134	-280 (-143)	-420 (-90)	-7.5
MAE (m)	172	379 (242)	523 (172)	205

Table 14: Statistical results for thermodynamic PBLH methods implemented on UAV (y) and MWR (x) profiles, for the 69 UAV profiles. The numbers in brackets are for comparisons made with only UAV profiles which reach a maximum height greater than the PBLH detected from the MWR profile. For the EI and SBLpT methods, this condition was met for all the UAV profiles. The SBLpT method was applied for profiles at all times of day, rather than just nocturnal profiles. Note that for the SBLpT method, the number in the P_{250} row is actually P_{100}.

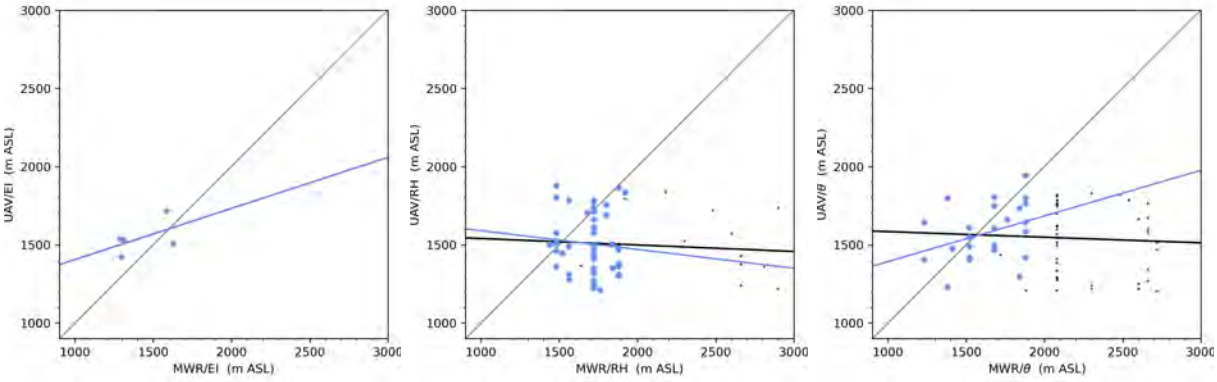

(a) (b) (c)

Figure 24: Comparison of PBLH detected by UAV and MWR profiles. Points in blue are those for which the maximum height reached by the UAV is greater than the PBLH detected from the MWR profile. The grey line is the 1:1 line. The black and blue lines are linear regressions of all points and blue points only respectively.

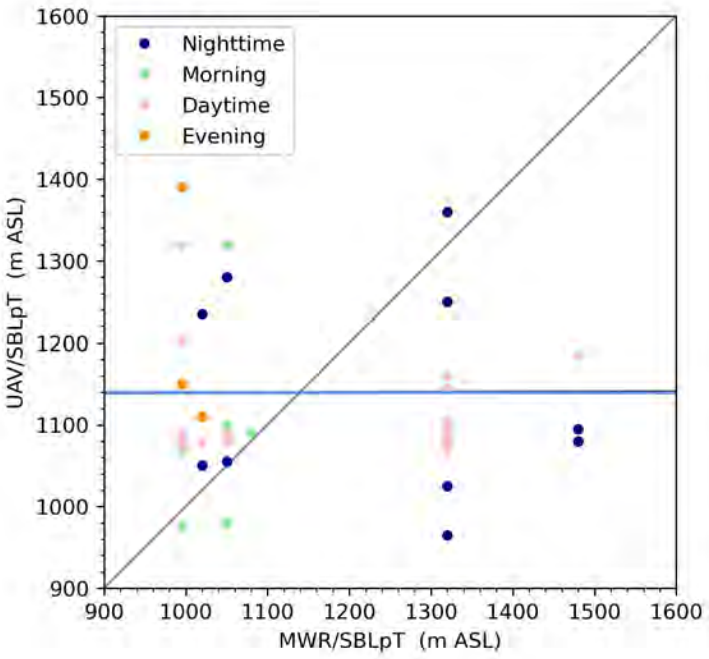

Figure 25: Comparison of MWR and UAV for the SBLpT method. The grey line is the 1:1 line. The blue line is the linear regression with all points. Points are coloured according to the time of day relative to sunrise, as defined in table 4.

C.2 Comparisons Without Low-level Clouds

Figures 26, 27, 28 and 29 show the same comparisons as figures 13, 14, 19 and 20 respectively, with all time points with cloud bases below 5000 m ASL removed. The effect of this cloud filter is discussed in section 5.2.2 and 5.3.3.

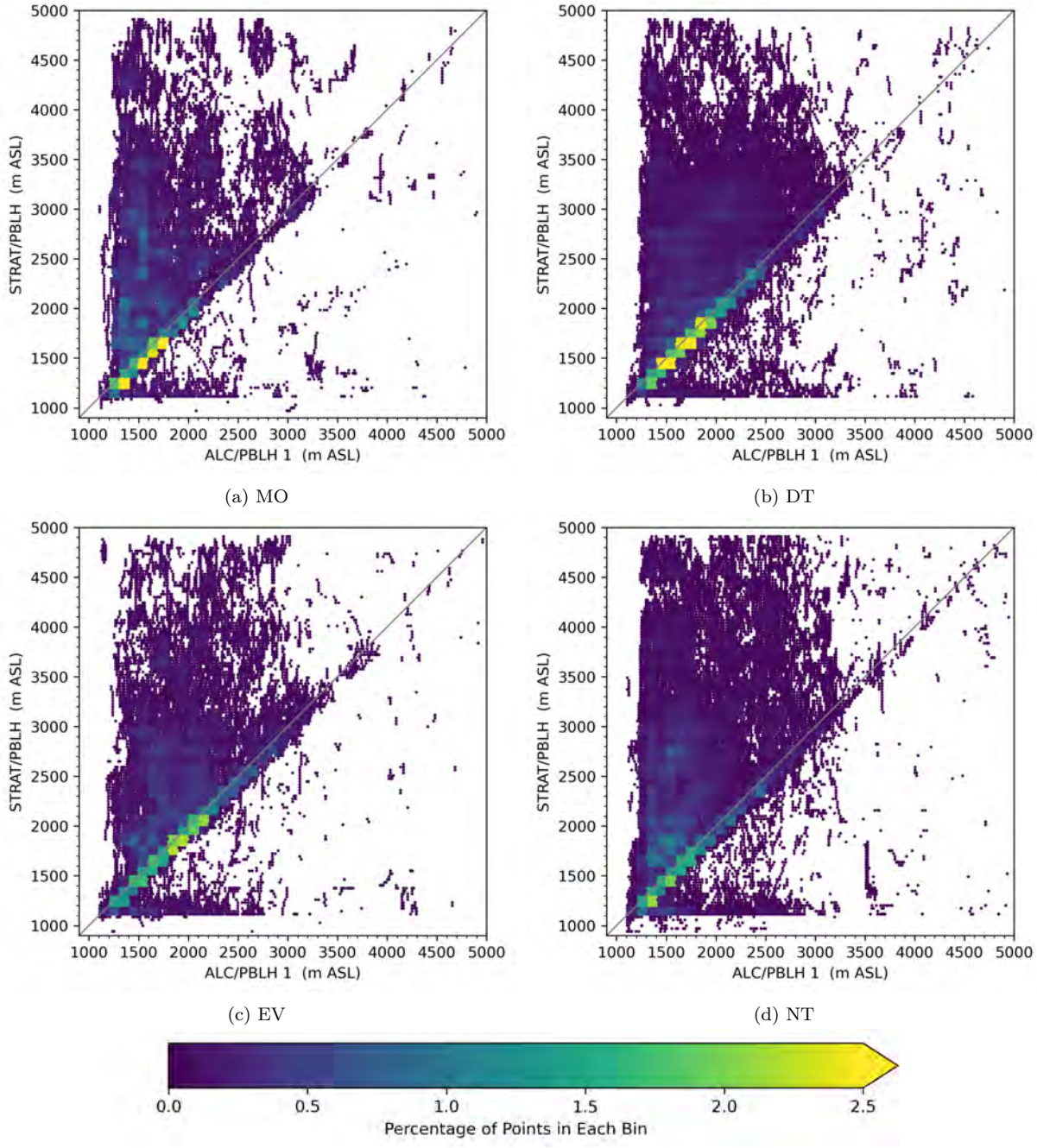

(a) MO

(b) DT

(c) EV

(d) NT

Figure 26: Comparison of STRAT/PBLH and ALC/PBLH with time points at which the cloud base height is below 5000 m ASL removed. Points are coloured according to the percentage of the points in each time division that lie within each 100 m by 100 m bin. The grey line indicates the 1:1 line.

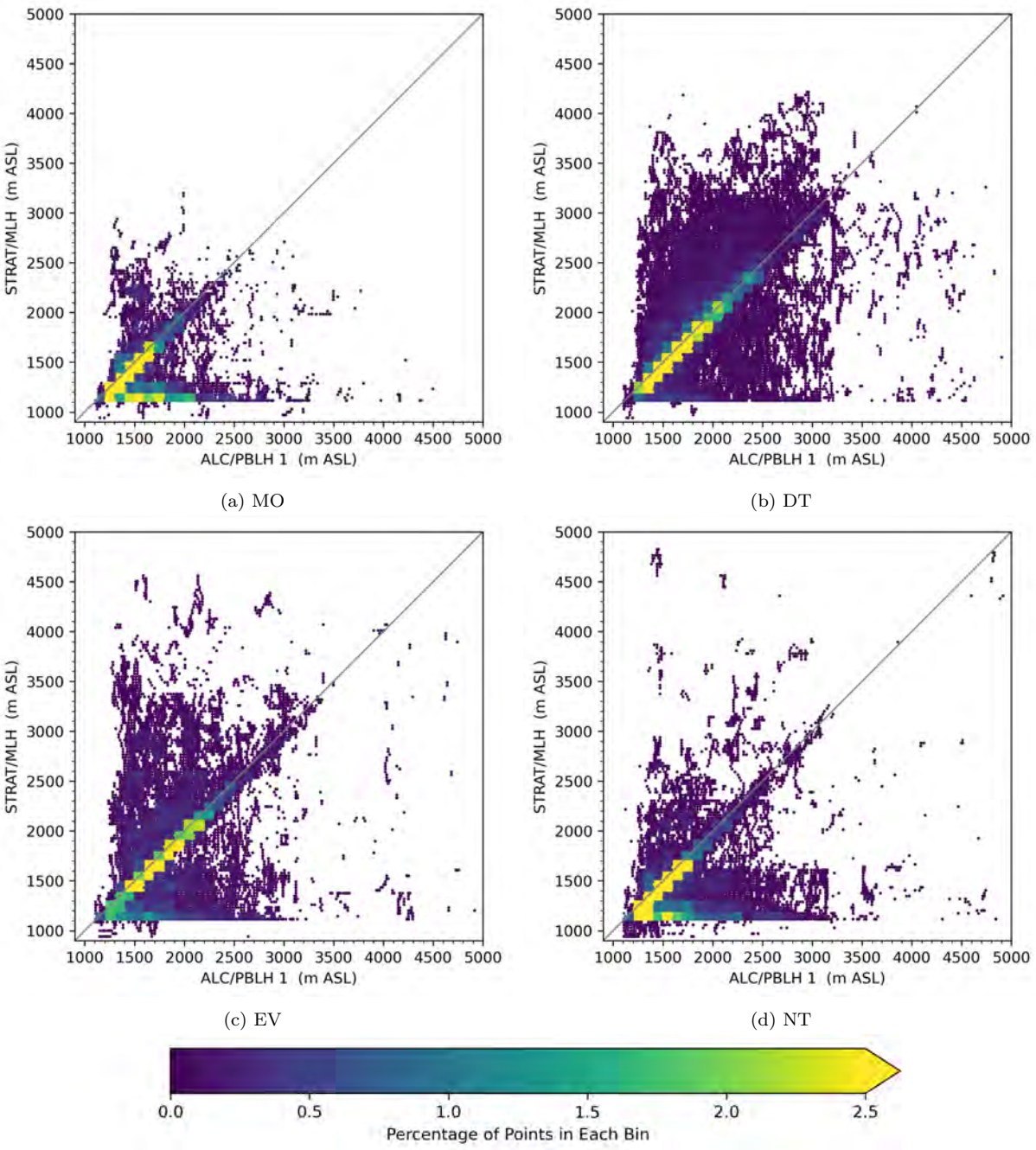

(a) MO

(b) DT

(c) EV

(d) NT

Figure 27: Comparison of STRAT/MLH and ALC/PBLH, with time points at which the cloud base height is below 5000 m ASL removed. Points are coloured according to the percentage of the points in each time division that lie within each 100 m by 100 m bin. The grey line indicates the 1:1 line.

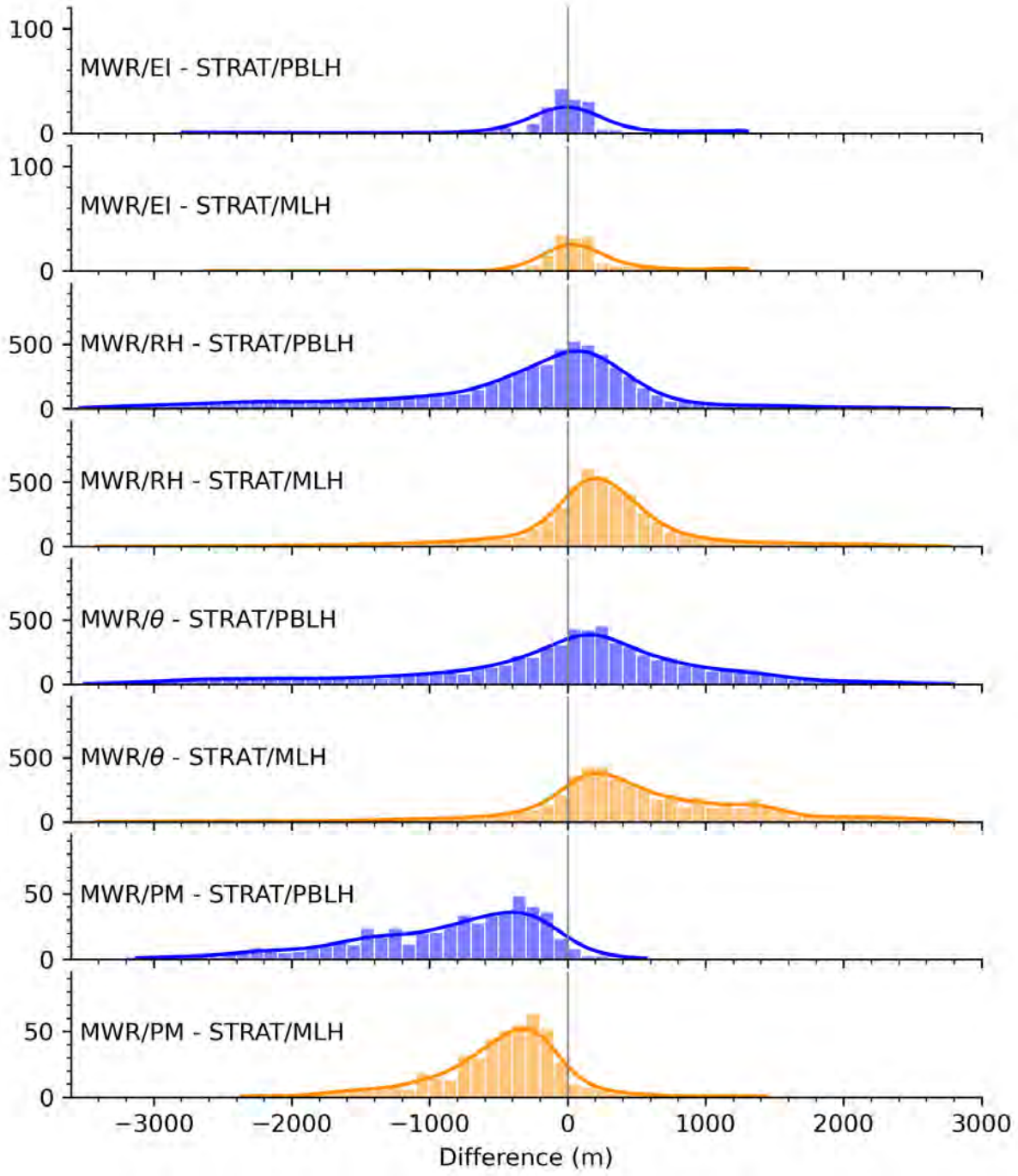

Figure 28: Comparison of STRAT/PBLH (blue) and STRAT/MLH (orange) to thermodynamic methods applied to the MWR, with time points at which the cloud base height is below 5000 m ASL removed. The y axis in each case is the count of observations in each 100 m interval, with the same scale as figure 19. The line indicates an approximate density function based on a Gaussian kernel density estimation function.

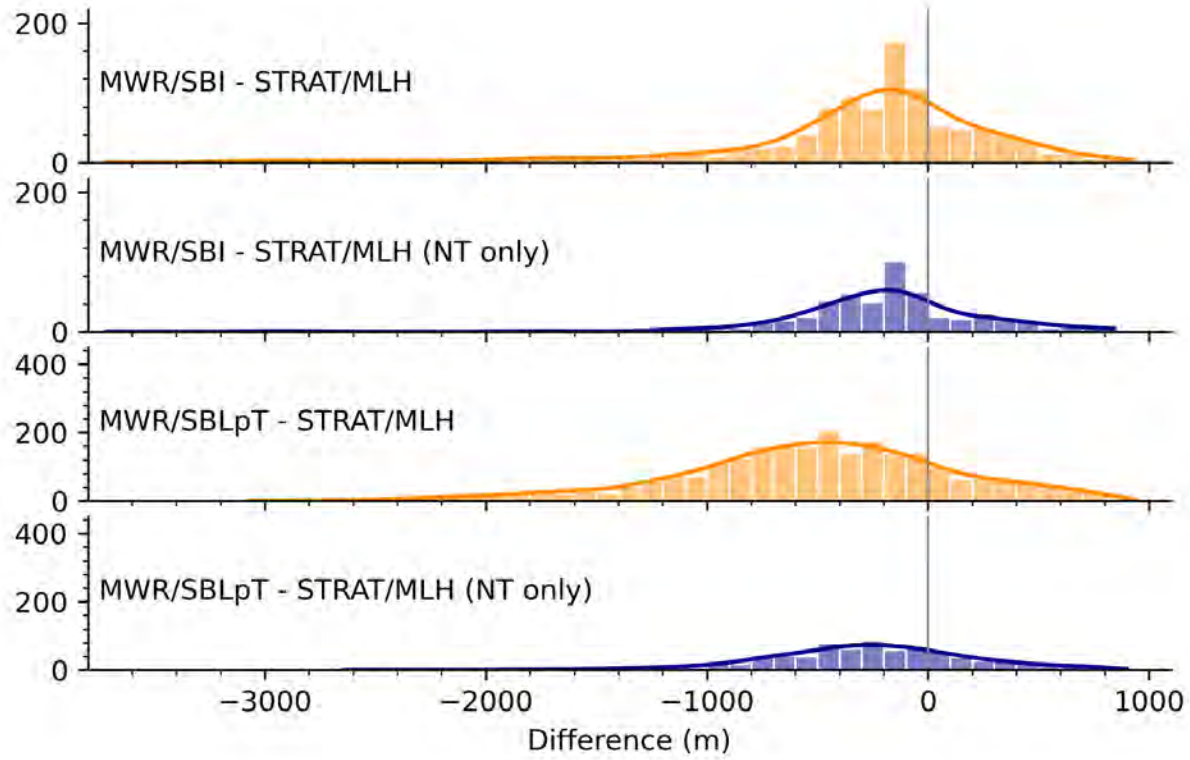

Figure 29: Comparison of STRAT/MLH to the nocturnal SBL methods methods applied to the MWR, at all times (orange) and at night only (dark blue), with time points at which the cloud base height is below 5000 m ASL removed. The y axis in each case is the count of observations in each 100 m interval, with the same scale as in figure 29. The line indicates an approximate density function based on a Gaussian kernel density estimation function.

Declaration of consent

on the basis of Article 30 of the RSL Phil.-nat. 18

Name/First Name: Corden, Heather Anne

Registration Number: 21-123-617

Study program: MSc in Climate Sciences

Bachelor ☐ Master ☑ Dissertation ☐

Title of the thesis: Investigating the Planetary Boundary Layer Height at the CLOUDLAB Field Site

Supervisor: PD. Dr. Gunter Stober (Institute of Applied Physics, University of Bern)
Dr. Robert Spirig (Institute of Atmosphere and Climate, ETH Zürich)

I declare herewith that this thesis is my own work and that I have not used any sources other than those stated. I have indicated the adoption of quotations as well as thoughts taken from other authors as such in the thesis. I am aware that the Senate pursuant to Article 36 paragraph 1 litera r of the University Act of 5 September, 1996 is authorized to revoke the title awarded on the basis of this thesis.

For the purposes of evaluation and verification of compliance with the declaration of originality and the regulations governing plagiarism, I hereby grant the University of Bern the right to process my personal data and to perform the acts of use this requires, in particular, to reproduce the written thesis and to store it permanently in a database, and to use said database, or to make said database available, to enable comparison with future theses submitted by others.

Bern, 30/3/2023

Place/Date

Signature Heather Corden.